Doctoral Thesis

Theory of topological charge pumping by moiré pattern sliding

Department of Physics, Osaka University

Manato Fujimoto

2023

Table of Contents

Chapter 1

Introduction

1.1 Purpose of study

Moiré superlattices, or multilayer systems obtained by stacking two-dimensional materials with rotational lattice mismatch, have attracted considerable interest in recent years. An emergent spatial period induced by long-range moiré pattern can be manipulated by twist angle, and it strongly modifies the electric property. In low-angle twisted bilayer graphene (TBG), for example, Dirac fermions of graphenes are reconstructed into nearly-flat bands [1, 2, 3, 4, 5, 6, 7, 8, 9, 10, 11, 12], leading to strongly correlated phenomena such as superconductivity[13, 14, 15] and strongly correlated insulating states[16, 15]. Moiré superlattices have been studied in various 2D materials, including graphenes[1, 2, 3, 4, 5, 6, 7, 8, 9, 10, 11, 12, 17, 18, 19, 20, 21], transition metal dichalcogenides[22, 23, 24, 25, 26, 27, 28, 29, 30, 31], 2D magnets[32, 33, 34, 35, 36, 37, 38], and semiconductors[39, 40, 41, 42, 43, 44], where unsual physical proeprties have been predicted and observed.

The stacked 2D materials have two interlayer structural degrees of freedom, twist (rotation of one layer to the other) and slide (translational shift). Unlike a twist, a slide does not change the long-range moiré period, but it entirely translates the whole moiré pattern in much faster speed than the layer sliding, as shown in Fig. 1.1. So far, little attention has been paid to the effect of sliding in the moiré superlattices. In this thesis, we highlight a dynamic consequence of relative shift for the electronic structure. The interlayer sliding process is cyclic in that a slide by a single atomic constant shifts the moiré pattern exactly by a

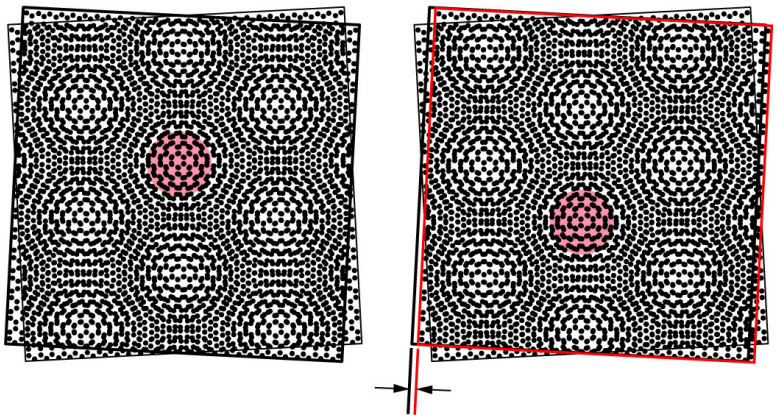

Figure 1.1: Moiré pumping in twisted bilayer graphene. From left to right, we slide layer 1 by half of the atomic constant, and then the moire pattern shifts by half of the moiré period as indicated by a pink circle.

single superlattice period. We study the electric current driven by the mechanical shift of the moiré pattern. We show that the electrons follow the movement of the moiré pattern, and the number of pumped charges in the interlayer sliding process is quantized into a topological invariant, which is dubbed as a sliding Chern number. Another major finding is the bulk-edge correspondence of the moiré pattern sliding. Here we calculate the electronic structure of finite-sized TBG and show that non-zero sliding Chern number dictates the existence of edge states in an analogous manner to the quantum Hall system.

The thesis is organized as follows. In the rest of this chapter, we will review the previous works on moiré superlattices and topological pumping. Chapter 2 provides theoretical basis to describe topological charge pumping and the band structure of TBG. In Chapter 3, we apply the theoretical methods to TBG, and study topological charge pumping in interlayer sliding. In Chapter4, we study the moiré edge states in TBG, and argue about the relationship to the sliding Chern number. We conclude the thesis in Chapter 5.

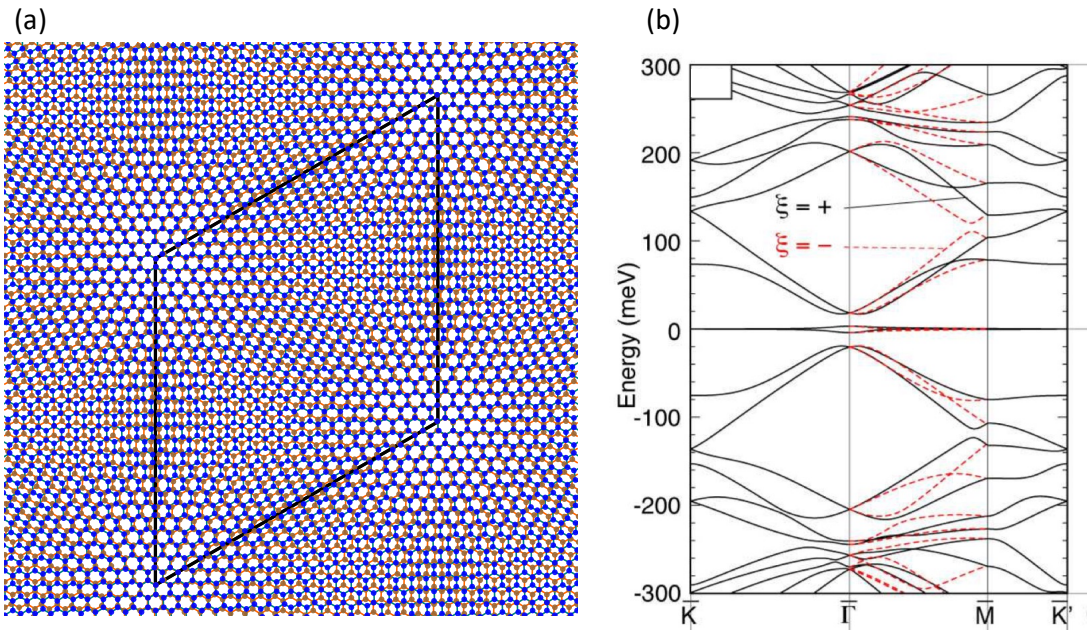

Figure 1.2: (a) The lattice structure of TBG for $\theta = 2.65°$ (b)The black and the red line represent the energy spectrum of magic angle TBG for K and K' valley, respectively.

1.2 Twisted bilayer graphene

1.2.1 Magic angle twisted bilayer graphene

Graphene is a two-dimensional crystal consisting of carbon atoms arranged in a honeycomb lattice and it was synthesized by the mechanical exfoliation of graphite into a single layer[45]. Graphene exhibits an extraordinarily high electron mobility as a consequence of the suppression of backscattering. This feature follows directly from the massless Dirac band with a linear energy-momentum relation, where the conduction and valence bands near the K and K' points touch at one degenerate point.

Twisted bilayer graphene (TBG) is composed of a pair of graphene layers rotationally stacked with a twist angle θ. The two isolated layers of graphene are assembled by weak van der Waals interaction without chemical bonds between layers. The local structure of the bilayer periodically varies in the real space with a moiré superlattice period $a/\sin(\theta/2)$, where $a \approx 0.246$ nm is graphene's lattice

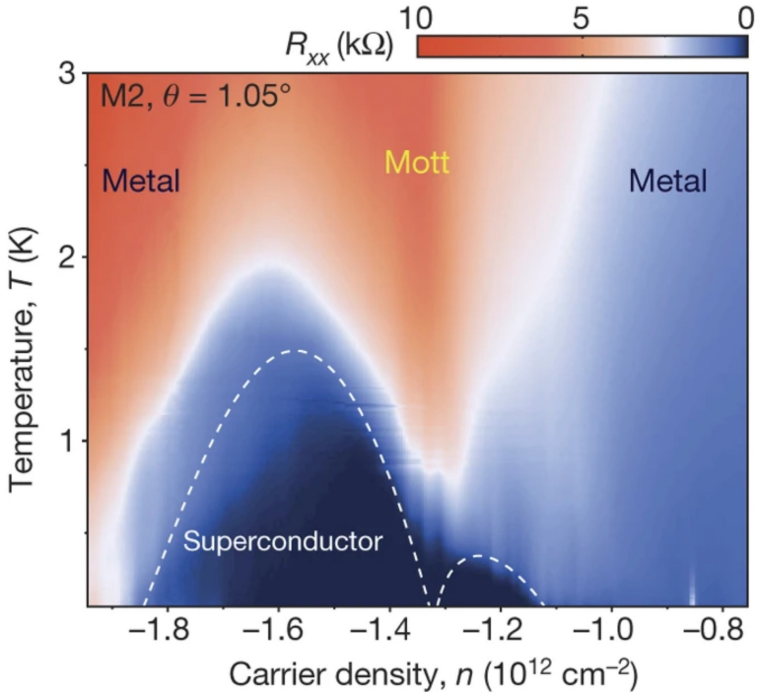

Figure 1.3: Mott insulating phase and superconducting phase of magic angle TBG[13]

constant. The superlattice encompasses more than ten thousand carbon atoms around 1°. The moiré pattern acts as a long-wavelength modulating potential, and dramatically affects electronic properties [1, 2, 3, 4, 5, 6, 7, 8, 9, 10, 11, 12].

The electronic band structure in TBG strongly depends on the twisted angle. When $\theta > 10°$, the two Dirac cones remain nearly intact in a low-energy regime. In decreasing θ, the moiré interlayer interaction suppresses the Fermi velocities, and a nearly flat band is achieved at $\theta = 1.1°$, which is called the magic angle. Figure 1.2 shows the band structure at the magic angle $\theta \approx 1.1°$ on high-symmetry lines in the Brillouin zone of TBG, where we see narrow bands isolated in energy around the charge neutrality point. Due to the weak spin-orbit interaction and inter-valley interaction, the flat bands are four-fold degenerate in spin and valley (K and K') degrees of freedom.

The narrow band implies that the electron-electron interaction plays a dominant role in the electronic properties, and hence the magic angle twisted bilayer graphene (MATBG) has been predicted to be an ideal platform to study

strongly correlated phenomena by [6]. In 2018, the MATBG was successfully fabricated, where a correlated insulating state was found at an integer filling of flat band [16], and also superconductivity is observed at slightly higher and lower doping from the correlated insulating state [13]. Figure 1.2 is a phase diagram of MATBG which shows a superconducting dome surrounding the insulating state. The apparent resemblance to that of high-T_c cuprates has attracted theoretical and experimental researchers to understand the mechanism of the phenomena. Moreover, the unexpected physics ignited intense theoretical study about a bunch of features of this system, such as irreducible symmetries [46, 47, 48, 49, 50, 51], pairing mechanism and symmetry of the superconducting phase [52, 53, 54, 55, 56, 57, 58, 59, 60, 61, 61, 62] and additional magic angles [63].

1.2.2 Other moiré materials

Generally, moiré pattern is formed by an interlayer rotation or a small lattice mismatch, and it has been found in various 2D materials. In particular, hexagonal boron nitride (hBN) and transition metal chalcogenide (TMDC) are representative materials as components of moiré superlattices. They have honeycomb lattices like graphene, while asymmetry of A and B sublattices breaks spatial inversion symmetry, leading to characteristic electric properties different from twisted bilayer graphene.

The twisted bilayer of h-BN has the AB-stacking region where boron sites are located above nitrogen sites and the BA-stacking region with nitrogen above boron, creating a staggered polarization of the AB and BA domains [42, 43, 44]. The spontaneous out-of-plane charge polarization means twisted bilayer hBN has ferroelectricity. The moiré pattern can be visualized by Piezo-force microscopy (PFM) as shown in Fig 1.4(b). The ferroelectricity persists in room temperature, and it is expected to be applied to a potential ultrathin nonvolatile memory.

At a small twist angle, twisted bilayers of TMDC also exhibit isolated flat

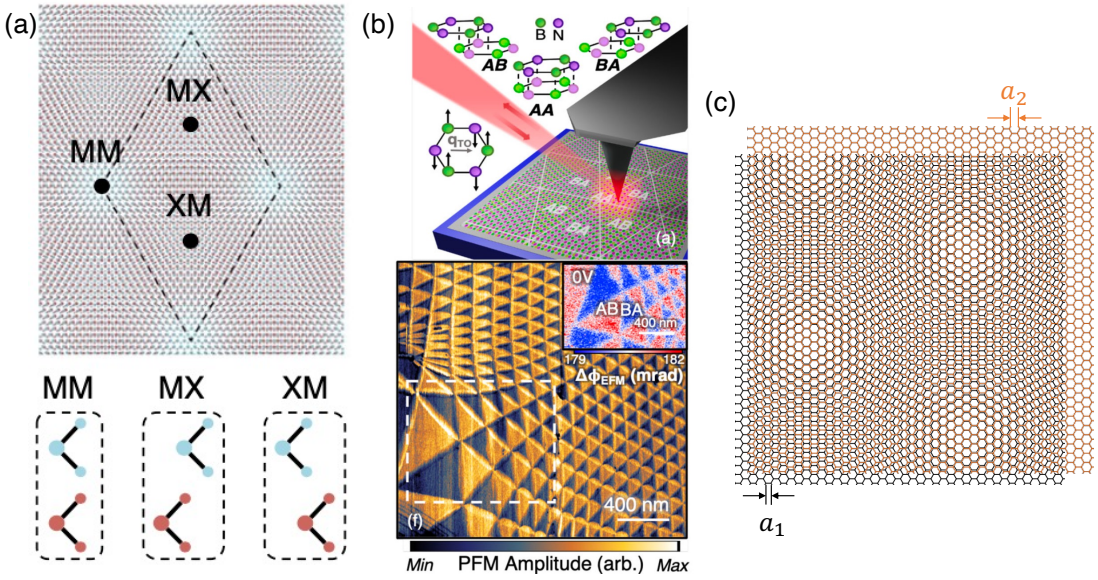

Figure 1.4: (a)Moiré superlattice of twisted homobilayer TMD. The bottom panels show the cross-section views of the high-symmetry sites (MM, MX and XM). The large and small dots represent the transition metal atom and the chalcogen atom, respectively.[64] (b)The upper panel is a schematic picture of twisted hexagonal Boron Nitride and its representative stacking configurations (AA, AB, BA). Their experiments captured a triangular superlattice in the lower panel by Piezo-force microscopy.[44] (c)non-twisted graphene and hexagonal boron nitride. The lattice mismatch is exaggerated as $a_2/a_1 = 10/9$.

bands, providing a powerful platform for the investigation of Hubbard model physics on an emergent lattice.[23, 28, 29, 30] The effective model is composed of low-energy electronic orbitals located at MX and XM spots in the moiré unit cell (Fig. 1.4(a)[64]). Additionally, the non-equivalent MX and XM sublattice sites provide a realization of the Kane-Mele model. The combination of non-trivial topology and electric correlation is anticipated to support a plethora of exotic electronic states of matter.

Moiré superlattices generated from different types of 2D materials are called heterobilayers. A representative example is graphene on h-BN (Fig.1.4(c)), and its moiré pattern was actually observed by scanning tunneling microscopy.[65, 66, 67, 68] The graphene on h-BN system has been extensively studied theoretically[69, 70, 71, 72] and experimentally, where secondary Dirac points,[73, 74, 75], the Hofstadter butterfly,[73, 74, 75, 76, 77], Brown-Zak oscillations [73, 74, 75, 76, 77, 78] have been observed. The heterobilayer of TMDC can host interlayer excitons, in which the optically excited electrons and holes reside in different layers.[25, 26, 22, 27, 31] While the radiative lifetime of single-layer excitons is picosecond timescales, that of the moiré excitons was observed to be hundreds of nanoseconds.[25, 26, 22, 27, 31]

The moiré effect has also been studied on various physical phenomena other than electronic properties. It was predicted that acoustic phonon modes of TBG are reconstructed into moiré phonon, corresponding to effective oscillations of the moiré pattern.[79, 80, 81, 82, 83, 84] Such modifications of phonon bands are expected to strongly affect the electronic[52, 56, 85, 86] and thermal transport[87, 88] properties. Another platform for moiré physics is magnetic 2D materials such as chromium trihalides (CrX3, X = I, Br, and Cl).[32, 33, 34, 35, 36, 37, 38] In particular, moire superlattices of CrCl3/MnPS3, CrBr3/MnPSe3, and CrI3/MnPTe3 are proposed to host magnetic skyrmions.[32]

1.3 Quantum pump

1.3.1 Topological charge pump

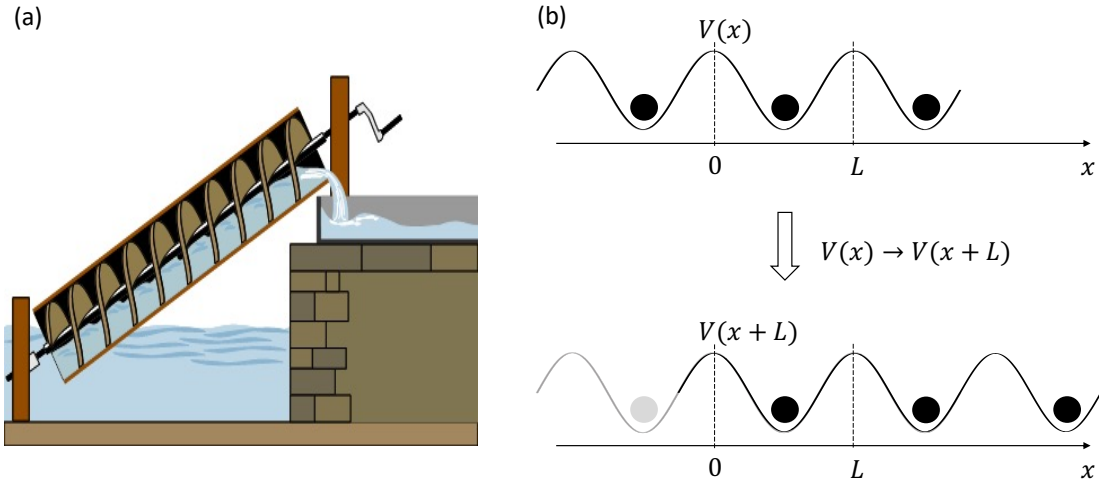

Figure 1.5: (a) Schematic picture of Archimedean screw (https://mechstuff.com/amazing-archimedean-screw/) (b)The black dots adiabatically follow the valley of the potential. If the potential is slid by its period L, the system returns to its original state (lower panel). The gray dots represent the position of the black dots before a cycle.

A pump is a device that moves liquid by external manipulation. Figure 1.5 shows one of the oldest pumps, called the Archimedean screw pump, which is a mechanical device to pump up water by a rotating spiral blade. The machine converts the cyclic motion of the blade to a directed motion of water, and at each full turn of the pump, the transferred volume is identical no matter how slowly the screw is rotated.

A quantum mechanical analog of the device is the topological charge pump (Thouless pump), which was first proposed by Thouless [89]. When the process is adiabatic, i.e. a cyclic variation of the potential is slow enough for the particles to follow the dynamics, the amount of the transferred particles are precisely quantized. In the general formulation of topological charge pumping, we consider a time-dependent Bloch Hamiltonian which has periodicities in space and in time. The number of transferred electrons is quantized to a two-dimensional topological

invariant, given by a Chern number:

$$C = \sum_{n\in\text{occ}} \int_{\text{BZ}} \frac{dk}{2\pi} \int_0^T dt \left(\frac{\partial}{\partial k} \left\langle \psi_{nk}(t) \left| i\frac{\partial}{\partial t} \right| \psi_{nk}(t) \right\rangle - \frac{\partial}{\partial t} \left\langle \psi_{nk}(t) \left| i\frac{\partial}{\partial k} \right| \psi_{nk}(t) \right\rangle \right) \tag{1.1}$$

where $|\psi_{nk}\rangle$ is the Bloch state of energy band n at the Bloch wavenumber k, BZ stands for the first Brillouin zone, and $\sum_{n\in\text{occ}}$ represents the summation over all occupied bands. Therefore the topological charge pump is robust against perturbations. Figure 1.5(b) shows an example of a topological charge pump. We consider electrons trapped by a periodic potential, where each potential minimum accommodates a single electron. When the potential is adiabatically translated by a single spatial period, the electrons naturally follow the motion of potential, and thus the number of pumped electrons per cycle is one, i.e., $C = 1$.

The observation of quantum pumping was recently accomplished using ultracold atoms in optical lattices[90, 91, 92] and it was also extensively studied in theory.[93, 94, 95, 96, 97, 98, 99] In this thesis, we propose the realization of the topological pumping by an interlayer sliding of TBG.

1.3.2 Quantum Hall effect (QHE)

The Chern number also describes the quantum Hall effect (QHE) in 2D quantum electrons in a strong magnetic field.[100] The QHE can be viewed as a static analog of the Thouless pumping from the following Laughlin's gedanken experiment.[101, 102]

Let us consider a 2D electron gas confined to a ribbon that is finite in the x direction and periodic in the y direction, and we apply a uniform magnetic field B perpendicular to the 2D plane. The system is equivalent to a cylinder as shown in Fig. 1.6(a), where the magnetic field B is radially penetrating the cylinder surface. We adiabatically thread a fictional flux Φ through the cylinder independently of the field B. The time-dependent flux gives rise to an electric

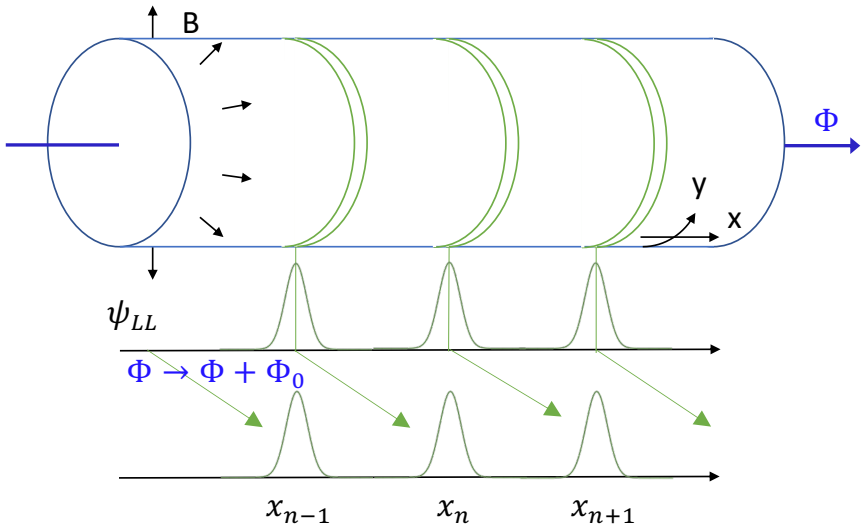

Figure 1.6: Schematic picture of Laughlin cylinder. The magnetic field is perpendicular to the sample. The inserted flux Φ changes k_y to $k_y + \Phi$, leading to the shift of the center of a Landau-level wavefunction.

field $E_y = -d\Phi/dt$ along y direction, and the associated electronic movement in x direction gives the Hall current $I_x = \sigma_{xy} E_y$.

In the presence of the magnetic flux Φ, the momentum k_y is shifted to $k_y \to k_y + \frac{2\pi}{L_y}\frac{\Phi}{\Phi_0}$ where $\Phi_0 = h/e$ and L_y is the circumference of the cylinder. This tells us that the inserting magnetic flux displaces the center of the Landau level (LL) wavefunctions $x_n = \Phi_0 k_y/(2\pi B) + n\frac{2\pi}{L_y}$ where n is the label of LL. As shown in the lower panel of Fig. 1.6, if we vary Φ by Φ_0, x_n is translated to x_{n+1} and then the system returns to its initial state. Because this sliding motion of the Landau levels can be considered as Thouless pumping, an integer number of electrons is transferred along x axis. If we define the number of pumped charges as N, the induced current can be written as

$$I_x = eN\frac{d}{dt}\frac{\Phi}{\Phi_0} = N\frac{e}{h^2}E_y. \tag{1.2}$$

The Hall conductivity σ_{xy} can be obtained from a straightforward application of linear response theory. Thouless and his coworker[100] showed that the integer

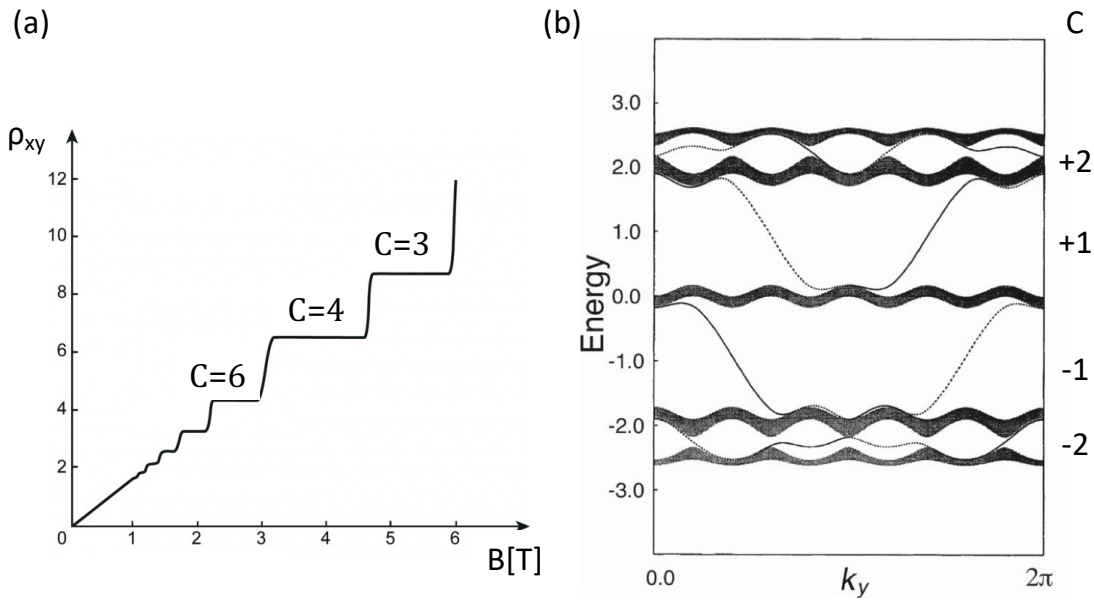

Figure 1.7: (a) Hall resistivity as a function of magnetic field (b) The energy spectrum for a ribbon of quantum Hall system. The shaded area represents the bulk bands. In the right row, the Chern number for each gap is written.[103]

N is precisely quantized to the Chern number

$$N = \sigma_{xy} / \left(\frac{e^2}{h}\right) = \sum_n \int_{BZ} \frac{d^2\mathbf{k}}{(2\pi)^2} \left(\frac{\partial}{\partial k_x} \left\langle \psi_{n\mathbf{k}} \left| i \frac{\partial}{\partial k_y} \right| \psi_{n\mathbf{k}} \right\rangle - \frac{\partial}{\partial k_y} \left\langle \psi_{n\mathbf{k}} \left| i \frac{\partial}{\partial k_x} \right| \psi_{n\mathbf{k}} \right\rangle \right). \tag{1.3}$$

The variation of magnetic flux Φ is incorporated as k_y. By the comparison of Eqs.(1.1) and (1.3), QHE can be interpreted as a static version of Thouless pump where the shift of k_y resulting from the inserted magnetic flux corresponds to the adiabatic and cyclic variation of the parameter t.

1.4 Topological edge states

1.4.1 Bulk-edge correspondence

One of the important aspects of the QHE is the emergence of edge states at the boundary of the sample.[104, 101, 105] The relation between the topological invariant defined in infinite systems and the edge states is known as *bulk-edge correspondence*. This occurs because of discontinuity of the topological num-

ber across the boundary between the topologically trivial and nontrivial phases. For example, Fig. 1.7(b) shows the energy spectrum for a ribbon structure of QHE model.[105] The number of edge states coincides with the Chern number written in the right row of Fig. 1.7(b). Recently, the concept of the bulk-edge correspondence has been extended to other symmetry classes and dimensions and found various topological boundary modes such as the Majorana edge state at the Kitaev chain[106], quantum spin Hall effect[107, 108], Dirac surface states on three-dimensional topological insulators[109], and corner state at higher-order topological insulators[110].

Due to the mathematical similarity to the quantum Hall system, the adiabatic charge pump is also related to the existence of edge states through the Chern number. From the equivalence of cyclic parameter t and wavenumber k_y, the edge states of the adiabatic charge pump connect the valence bands and conduction bands when plotted against t. The topologically protected boundary states were observed in 1D photonic waveguide[111] and have been studied theoretically in [112]

1.4.2 Edge states in twisted bilayer graphene

Some previous works studied the edge properties of TBG, showing that TBG has two kinds of edge states.[113, 114, 115, 116, 117, 118] One is zero-energy edge modes on the zigzag termination, [113, 114, 115, 116] originating from a feature of monolayer graphene related to nontrivial Berry phase of the Dirac cone [119]. The other one, which we refer to moiré edge state, is a qualitatively different state strongly dependent on the moiré pattern and occurs away from zero energy. Compared to Figs.1.8(α) and (β), the moiré edge states decay with moiré length scale while the zigzag edge states are strongly localized at the boundary of the sample. Around the magic angle, in particular, the moiré edge states come to the energy gaps between the flat band and the excited band.

One may ask if the moiré edge states are related to some sort of bulk topology.

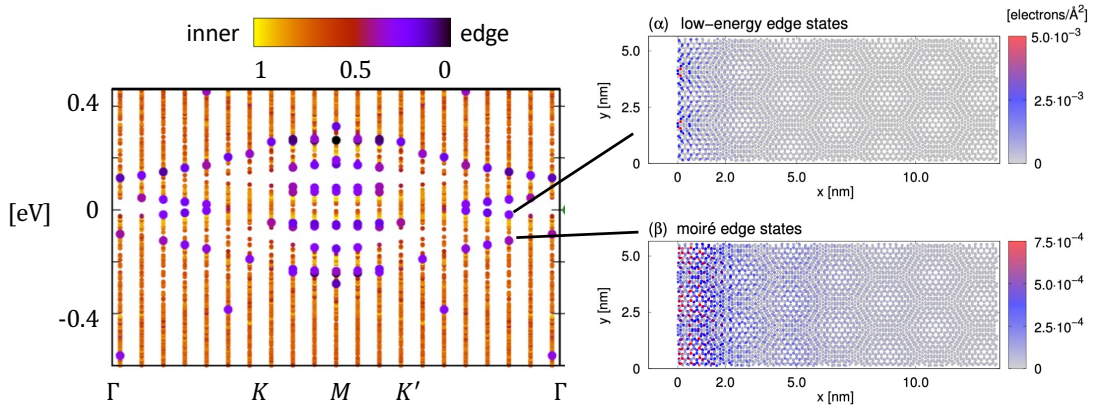

Figure 1.8: Energy spectrum of twist bilayer nanoribbon with $\theta = 2.3°$. The color of each energy band represents the expected value of x coordinate. The real space map of the wavefunction for (α)zero mode edge states (β)moiré edge states.[117]

The energy bands of TBG have zero Chern number, and hence the system does not have any edge states associated with the Hall effect or the valley Hall effect. Therefore, the exploration of a topological invariant characterizing the moiré edge state is still an open question.

Here, we investigate the edge states of the moiré system under the interlayer sliding and find that the emergence of the moiré edge states can be explained by the bulk-edge correspondence of sliding Chern numbers. We demonstrate the moiré edge states transferred in the moiré gap during the interlayer sliding process, and the number of edge states pumped in a sliding cycle is equal to the sliding Chern number of the band gap.

Chapter 2

Theoretical background

2.1 Charge pumping in 1D

Here, we introduce the fundamental theory for topological charge pumping. We first discuss how the geometric phase arises during the adiabatic evolution of a quantum state. Second, we introduce the adiabatic current for Bloch Hamiltonian with cyclic modulation. We show that the number of pumped charges for the one cycle can be expressed as a topological integer, so-called Chern number. We then explain the relationship between the number of pumped charges and the number of edge states, so-called bulk-edge correspondence, by exemplifying Aubry-Andre model.

2.1.1 Geometric phase under adiabatic process

We consider a single particle in a non-degenerate system with slowly modulated in time, satisfying the following time-dependent Shrödinger equation,

$$\hat{H}(\varphi(t))|\psi(t)\rangle = i\hbar\frac{\partial}{\partial t}|\psi(t)\rangle, \tag{2.1}$$

where the Hamiltonian is parametrized by $\varphi(t)$ and $|\psi(t)\rangle$ is the wave function. Using the eigenvector of the Hamiltonian $|u_n(t)\rangle$ at fixed time t,

$$\hat{H}(\varphi(t))|u_n(t)\rangle = E_n(t)|u_n(t)\rangle, \tag{2.2}$$

and form a complete basis. so that the ansatz of Eq.(2.1) can be expanded as

$$|\psi(t)\rangle = \sum_m c_m(t) e^{-\frac{i}{\hbar}\int_0^t \mathrm{d}t' E_m(t')} |u_m(t)\rangle. \tag{2.3}$$

The coefficients satisfy

$$\dot{c}_m(t) = -c_m(t)\left\langle u_m(t)\left|\frac{\partial}{\partial t}\right|u_m(t)\right\rangle - \sum_{l\neq m} c_l(t) e^{-\frac{i}{\hbar}\int_0^t \mathrm{d}t'(E_l - E_m)}\left\langle u_m(t)\left|\frac{\partial}{\partial t}\right|u_l(t)\right\rangle \tag{2.4}$$

The second term representing the hybridization of the different energy states is neglected in adiabatic evolution, as shown below. By using the derivative of Eq.(2.2) by t:

$$\langle u_m(t)|\dot{H}|u_l(t)\rangle + E_m\langle u_m(t)|\frac{\partial}{\partial t}|u_l(t)\rangle = E_l\langle u_m(t)|\frac{\partial}{\partial t}|u_l(t)\rangle, \tag{2.5}$$

under adiabatic evolution, we obtain[120].

$$\left\langle u_m(t)\left|\frac{\partial}{\partial t}\right|u_l(t)\right\rangle = \langle u_m(t)|\frac{\dot{H}}{E_l - E_m}|u_l(t)\rangle \sim 0. \tag{2.6}$$

Finally, we solve Eq.(2.4) as

$$c_m(t) = e^{-\int_0^t \mathrm{d}t'\langle u_m|\partial_{t'}|u_m\rangle} c_m(t=0). \tag{2.7}$$

Therefore, The particle will follow the eigenstate $|u_m\rangle$ and acquire a phase. Note that $\langle u_m|\frac{\partial}{\partial t}|u_m\rangle$ is pure imaginary, as

$$\langle u_m|\frac{\partial}{\partial t}|u_m\rangle = \left(\frac{\partial}{\partial t}\langle u_m|\right)|u_m\rangle = -\langle u_m|\frac{\partial}{\partial t}u_m\rangle. \tag{2.8}$$

$A_m(\varphi) = \langle u_m|\partial_\varphi|u_m\rangle$, called Berry connection, is gauge-dependent. A gauge transformation $|u_m\rangle \to e^{i\chi(\varphi)}|u_m\rangle$ with $\chi(\varphi)$ an arbitrary smooth function transforms the berry connection as $A_m(\varphi) \to A_m(\varphi) - \frac{\partial}{\partial\varphi}\chi(\varphi)$ and the phase of c_m is changed by $\chi(\varphi(T)) - \chi(\varphi(0))$, where $\varphi(0)$ and $\varphi(T)$ are the initial and final

parameter of the process. Thus, one can always choose a suitable gauge such that the phase accumulation is canceled out along the process.[121] However, for the adiabatic modulation along a closed loop in the parameter space $\varphi(T) = \varphi(0)$, the phase becomes a gauge-invariant physical quantity because of a single-valued χ, which implies $\chi(\varphi(T)) - \chi(\varphi(0)) = 2\pi \times$ (integer). It is known as the Berry phase or geometric phase, given by

$$\gamma_m = \oint \mathrm{d}\varphi A_m(\varphi). \tag{2.9}$$

To calculate the current of the particle under an adiabatic process, the second term of Eq.(2.4) should be taken into account. We decompose the coefficient c_m into the zeroth order $c_m^{(0)}$ and the first order $c_m^{(1)}$ with respect to the derivative by t. Due to the initial condition, $c_m(0) = \delta_{m,n}$, only contributions from the initial state $|u_n\rangle$ have to be taken into account in Eq.(2.4). Finally, we obtain

$$c_n^{(0)}(t) = e^{i\left(\gamma_D^{(n)} + \gamma_B^{(n)}\right)} \tag{2.10}$$

and

$$c_m^{(1)}(t) = i\hbar e^{i\gamma_B^{(n)}(t)} e^{i\left(\gamma_D^{(n)} - \gamma_D^{(m)}\right)} \frac{\langle u_m(t)|\frac{\partial}{\partial t}|u_n(t)\rangle}{E_m - E_n} \tag{2.11}$$

where $\gamma_D^{(m)} = -\frac{1}{\hbar}\int_0^t \mathrm{d}t' E_m$ is referred to as the dynamical phase. Therefore, Eq.(2.3) can be written as

$$|\psi(t)\rangle = e^{i\left(\gamma_D^{(n)} + \gamma_B^{(n)}\right)} \left(|u_n(\varphi)\rangle + i\hbar \frac{\partial \varphi}{\partial t} \sum_{m \neq n} \frac{\langle u_m(\varphi)|\frac{\partial}{\partial \varphi}|u_n(\varphi)\rangle}{E_m - E_n} |u_m(\varphi)\rangle \right) \tag{2.12}$$

The second term plays a significant role in transport under adiabatic transport as shown in the next section.

2.1.2 Geometric charge pumping

A Thouless charge pump can be implemented in the one-dimensional system which is spatial periodic and cyclic, i.e., the Hamiltonian satisfies

$$\hat{H}(x,\varphi(t)) = \hat{H}(x+L,\varphi(t)) \tag{2.13}$$

$$\hat{H}(x,\varphi(t)) = \hat{H}(x,\varphi(t+T)). \tag{2.14}$$

In this case, the wavefunction can be decomposed cell-periodic part of the wave function and complex phase as $\psi_{n,k_x} = e^{ik_x x}u_{nk_x}(x)$ where n is band index and $\hbar k_x$ is crystal momentum. The dynamics of the single particle is described by the time-dependent Bloch Hamiltonian $\hat{H}\left(k_x,\varphi\right) = \langle u_{nk_x}\left(\varphi\right)|\hat{H}|u_{nk_x}\left(\varphi\right)\rangle$. Because of the periodicity for $k_x(-\pi/L \leq k_x \leq \pi/L)$ and $\varphi(0 \leq \varphi \leq 2\pi)$, the Hamiltonian is defined on the quasi-Brillouin zone spanned by (k_x,φ).

In the Bloch basis, the expectation value of the velocity has the form $v\left(k_x,\varphi\right) = \partial\hat{H}\left(k_x,\varphi\right)/\hbar\partial k_x$. Using Eq.(2.12), the first order term becomes

$$v_n\left(k_x,\varphi\right) = \underbrace{\frac{1}{\hbar}\frac{\partial E_n\left(k_x,\varphi\right)}{\partial k_x}}_{v_{\mathrm{gr}}(k_x,\varphi)} + \underbrace{i\frac{\partial\varphi}{\partial t}\sum_{m\neq n}\left(\frac{\langle u_m|\frac{\partial}{\partial\varphi}|u_n\rangle}{E_m - E_n}\langle u_n|\frac{\partial\hat{H}}{\partial k_x}|u_m\rangle - \text{c.c.}\right)}_{v_{\mathrm{a}}(k_x,\varphi)} \tag{2.15}$$

where $|u_n\rangle = |u_{nk_x}\left(\varphi\right)\rangle$ for simplicity. The first term $v_{\mathrm{gr}}\left(k_x,\varphi\right)$ is the group velocity of the eigenstate obtained from the energy spectrum $E_n\left(k_x,\varphi\right)$. On the other hand, the second term $v_{\mathrm{a}}\left(k_x,\varphi\right)$ is called anomalous velocity resulting from the mixture of $E_n\left(k_x,\varphi\right)$.[122] By using

$$\frac{\langle u_n|\frac{\partial}{\partial k_x}\hat{H}|u_m\rangle}{E_m - E_n} = \langle u_n|\frac{\partial}{\partial k_x}u_m\rangle \tag{2.16}$$

the anomalous velocity can be written as

$$v_a\left(k_x,\varphi\right) = \sum_{n\in\mathrm{occ}}\Omega_n\left(k_x,\varphi\right)\frac{\partial\varphi}{\partial t} \tag{2.17}$$

where

$$\Omega_n\left(k_x,\varphi\right)=\frac{\partial}{\partial\varphi}A_n^{k_x}-\frac{\partial}{\partial k_x}A_n^{\varphi}=i\left(\langle\frac{\partial}{\partial\varphi}u_n|\frac{\partial}{\partial k_x}u_n\rangle-\langle\frac{\partial}{\partial k_x}u_n|\frac{\partial}{\partial\varphi}u_n\rangle\right) \tag{2.18}$$

is Berry curvature and

$$\boldsymbol{A}_n=(A_n^{k_x},A_n^{\varphi}),A_n^{k_x}=i\langle u_n|\frac{\partial}{\partial k_x}|u_n\rangle,A_n^{\varphi}=i\langle u_n|\frac{\partial}{\partial\varphi}|u_n\rangle \tag{2.19}$$

is Berry connection. Since v_a is proportional to $\frac{\partial}{\partial t}\varphi$, the contribution from anomalous velocity to pumping charge does not depend on the pumping speed. As shown in the following, it plays a significant role in generating a geometric charge pumping.

Let us consider the current for a homogeneously populated band which is calculated by integration of Eq.(2.15) over k_x. The periodicity of the energy spectrum $E_n(k_x+2\pi/L,\varphi)=E_n(k_x,\varphi)$ cancels out the current from the group velocity. Thus, the number of pumped charges during one cycle is

$$C=\frac{1}{2\pi}\int_{-\pi}^{\pi}\int_0^T\mathrm{d}k_x\mathrm{d}\varphi v_a=\sum_{n\in\mathrm{occ}}\frac{1}{2\pi}\oint\mathrm{d}k_x\mathrm{d}\varphi\Omega_n\left(k_x,\varphi\right), \tag{2.20}$$

called as Chern number which is one of the topological numbers.[89] The Chern number is topologically protected against perturbations that do not close the band gap. If the Berry connection is holomorphic in the whole regime of the quasi-BZ spanned by $\boldsymbol{\theta}=(k_x,\varphi)$, Eq.(2.20) can be transformed by Stokes' theorem as

$$C=\sum_{n\in\mathrm{occ}}\frac{1}{2\pi}\oint_{\partial S}\mathrm{d}\boldsymbol{\theta}\cdot\boldsymbol{A}_n\left(k_x,\varphi\right), \tag{2.21}$$

where ∂S represents the boundary of the quasi-BZ. If $\boldsymbol{A}_n$ is well defined in the whole of BZ, an integral of the $\boldsymbol{A}_n$ over the boundary of the BZ vanishes because the BZ forms torus. Nonzero values of the Chern number are consequences of the nontrivial structure of $\boldsymbol{A}_n$, where it has singularities at points in the BZ.[123] Here, we divide the BZ into two regions hosting different gauges as an example in

the case where we are free from the singularities. We now suppose that the two wavefunctions are related by a gauge transformation at the boundary between the two regions: $|u^{(1)}_{n,k_x}\rangle = \exp\left(i\chi_n(\boldsymbol{\theta})\right)|u^{(2)}_{n,k_x}\rangle$ and thus, $\boldsymbol{A}^{(1)}_n = \boldsymbol{A}^{(2)}_n + \frac{\partial}{\partial\theta}\chi_n(\boldsymbol{\theta})$. The Chern number can be calculated as

$$C = \sum_{n\in\mathrm{occ}} \frac{1}{2\pi} \oint_{\partial S_1} \mathrm{d}\boldsymbol{\theta} \cdot \boldsymbol{A}^{(1)}_n\left(k_x, \varphi\right) + \sum_{n\in\mathrm{occ}} \frac{1}{2\pi} \oint_{\partial S_2} \mathrm{d}\boldsymbol{\theta} \cdot \boldsymbol{A}^{(2)}_n\left(k_x, \varphi\right) \tag{2.22}$$

The torus does not have a boundary, so we have $\partial S_1 + \partial S_2 = \partial BZ = 0$ because they have the opposite orientation. Thus,

$$\begin{aligned} C &= \sum_{n\in\mathrm{occ}} \frac{1}{2\pi} \oint_{\partial S_1} \mathrm{d}\boldsymbol{\theta} \cdot \left(\boldsymbol{A}^{(1)}_n\left(k_x, \varphi\right) - \boldsymbol{A}^{(1)}_n\left(k_x, \varphi\right)\right) && (2.23) \\ &= \sum_{n\in\mathrm{occ}} \frac{1}{2\pi} \oint_{\partial S_1} \mathrm{d}\boldsymbol{\theta} \frac{\partial}{\partial\theta} \chi_n(\boldsymbol{\theta}). && (2.24) \end{aligned}$$

From the single-valuedness constraint of the wavefunction, it is required that the integral takes the discrete values of 2π. Therefore Chern number is always an integer.

2.1.3 Charge pumping and electric polarization

The electric polarization is defined by using the adiabatic electric current discussed in the former section as [122, 124, 125, 126].

$$J = \frac{1}{L}\frac{dP}{dt} = \frac{1}{L}\frac{\partial P}{\partial\varphi}\frac{d\varphi}{dt}. \tag{2.25}$$

On the other hand, electric current is given as

$$J = -e \sum_{n\in occ.} \frac{1}{2\pi} \oint_{BZ} dk_x v_n\left(k_x, \varphi\right) \tag{2.26}$$

where n is band index and $v_n(k_x, \varphi)$ is a group velocity of electron. From the above two equations, we derive

$$\frac{1}{L}\frac{\partial P}{\partial \varphi} = \sum_{n\in \mathrm{occ}} \frac{1}{2\pi} \oint_{BZ} dk_x \Omega_n(k_x, \varphi) \tag{2.27}$$

Moreover, when we use the periodic gauge, $|\psi_{n,k_x}\rangle = |\psi_{n,k_x+2\pi/L}\rangle$, the integration $\oint_{BZ} \frac{\partial}{\partial k_x} A_n^{\varphi}$ becomes zero so that the difference of the polarization is

$$P(\varphi_f) - P(\varphi_i) = \int_{\varphi_i}^{\varphi_f} d\varphi_x \left[\frac{eL}{2\pi} \sum_{n\in occ.} \oint_{BZ} \mathrm{d}k_x \frac{\partial}{\partial \varphi} A_n^{k_x} \right]. \tag{2.28}$$

Finally, electric polarization can be written as

$$P(\varphi) = \frac{eL}{2\pi} \sum_{n\in occ.} \oint \mathrm{d}k_x A_n^{k_x}. \tag{2.29}$$

Note that by using Eq.(2.27) and Eq.(2.20), we derive

$$CL = \frac{\Delta P}{e} \tag{2.30}$$

where $\Delta P = P(2\pi) - P(0)$. The number of the pumped electron is calculated from the difference for electric polarization while $\varphi : 0 \to 2\pi$.

2.1.4 Harper/Aubry-Andre model (AA model)

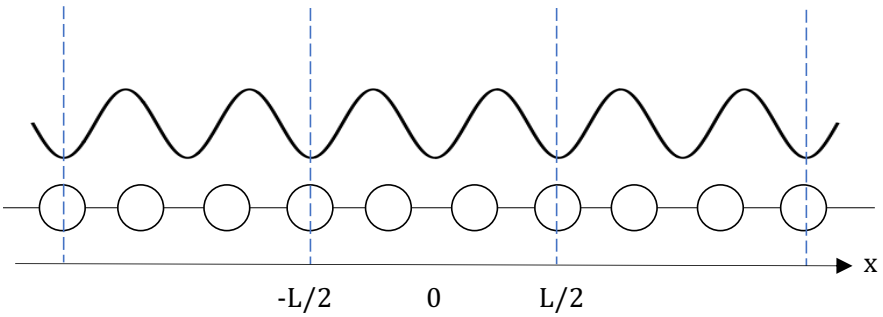

Figure 2.1: Schematic illustration of the AA model with $\alpha = 2/3$.

In this section, we show a method to analyze adiabatic transport from the

perspective of topology by exemplifying the Harper/Aubry-Andre model (AA model). The model is composed of a tight-binding chain with the nearest neighbor hopping J and sinusoidal potential with amplitude V_0. The Hamiltonian is written as

$$H(\varphi) = J\sum_i c_{i+1}^\dagger c_i + (h.c.) + V_0 \cos\left[2\pi\alpha\frac{iL}{N_s} + \varphi\right] c_i^\dagger c_i \tag{2.31}$$

where c_n is the single-particle annihilation operator at site n. α is the ratio of the number of periods of potential N_p to the number of atomic sites N_s in a single superlattice while φ is a phase. Figure 2.2(a) shows the calculated energy spectrum for $\alpha = 2/3, J = -1, V_0 = -2$ as a function of the modulation phase variation φ. The energy spectrum for discretized k_x has three isolated bands. As shown in Fig. 2.2 (b), the polarization for the lowest band is monotonically decreased with increasing φ and the variation of φ transfers -1 charge, which can be understood from Eq. (2.30).

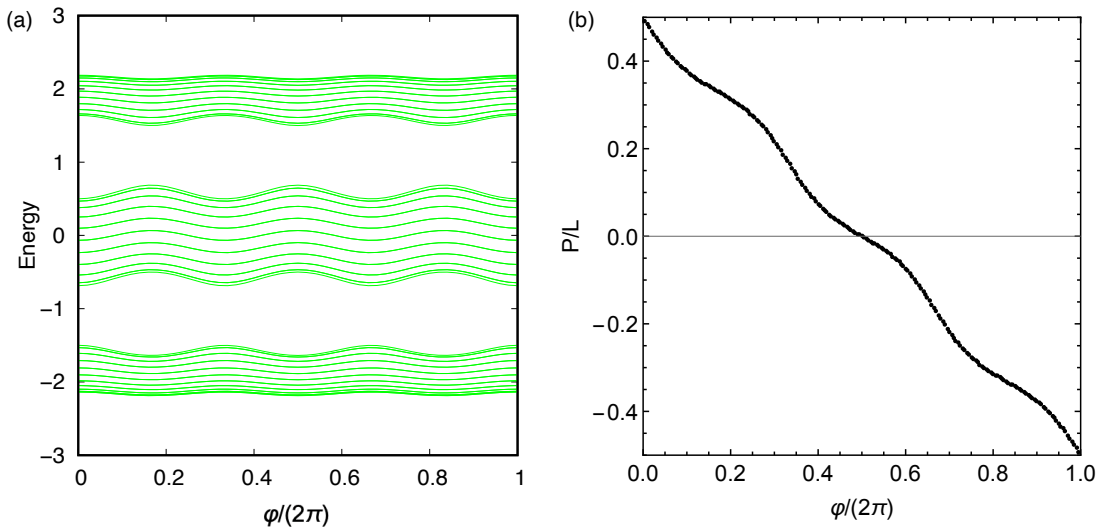

Figure 2.2: (a) the eigenenergy and (b) the polarization of lowest energy band calculated by Eq. (2.28) for $\alpha = 2/3, V_0 = -2$ with the modulation of φ

Here, we introduce an analytic method to calculate the Chern number by using an analogy to quantum Hall systems.[111] If we consider the variable phase φ as synthetic momentum orthogonal to the k_x-axis ($\varphi \leftrightarrow k_y$), the Hamiltonian [(2.31)]

is equal to a 2D tight-binding Hamiltonian defined as $\mathcal{H} = \int_0^{2\pi}(d\varphi/2\pi)H(\varphi)$, given by

$$\mathcal{H} = \sum_{i,j}\left[Jc^{\dagger}_{i,j}c_{i+1,j} + \frac{V_0}{2}e^{i2\pi\alpha i}c^{\dagger}_{i,j}c_{i,j+1} + \text{ h.c. }\right]. \tag{2.32}$$

Here we define $c_{i,\varphi} = \sum_j e^{-i\varphi j}c_{i,j}$ and $c_{i,\varphi}$ follows the commutation relation $\left\{c_{i,\varphi}, c^{\dagger}_{i',\varphi'}\right\} = \delta_{i,i'}\delta_{\varphi,\varphi'}$. This Hamiltonian describes a 2D square lattice fermion model under a magnetic field with α flux quantum per unit cell, named a Hofstadter-Harper (HH) Hamiltonian. Therefore, the number of pumped charges is the Chern number of the corresponding quantum hall system. The Chern numbers are known as the solution of the Streda formula,[127]

$$n = t + C\alpha, \tag{2.33}$$

where n is the electron density and t is an integer. By using the mathematical analog, we can rewrite it as

$$r = tN_p + CN_s, \tag{2.34}$$

where r is the number of occupied bands. One can compute the topological number without any k_x and φ dependence.

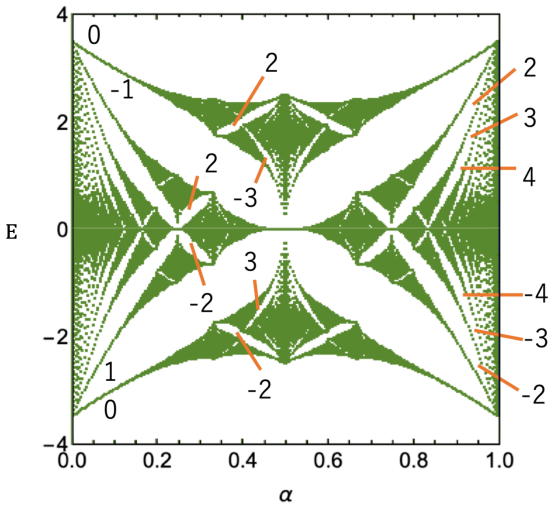

Figure 2.3: The spectral diagram of of HH Hamiltonian [Eq.(2.32)] for $J = -1$ and $V_0 = -3$. Each gap is labeled by the Chern number.

The energy spectrum of Hofstadter-Harper Hamiltonian (2.32) is well-known

due to hosting a fractal structure called the Hofstadter diagram.[128] Figure 2.3 shows the energy spectrum of Eq.(2.31) obtained by diagonalizing the Hamiltonian (2.31) by varying φ from 0 to 2π for rational values of α. Since the mathematical correspondence of φ of the AA model and k_y of the HH model, the energy structure of the AA model with the shift of φ ($0 \leq \varphi \leq 2\pi$) is as same as the HH model. The calculated Chern numbers correspond to the tangent of each gap as shown in Eq. (2.33) so that the plot of the diagram plays an important role to specify the topological feature.

2.1.5 Bulk-edge correspondence in topological charge pumping

If a two-dimensional bulk of an insulator has a non-zero Chern number such as a quantum Hall system, gapless edge modes emerge in the finite system. This relation is called bulk-edge correspondence. It is numerically and theoretically verified in the quantum Hall system [105, 129] and the other system [106, 130, 107, 131, 108, 109]. The emergence of a topological edge mode has been also confirmed in adiabatic charge pumping.[112, 91, 90]

In this section, we discuss bulk-edge correspondence for topological charge pumping by using the AA model.[112]. We consider a system with an open boundary condition: $|\psi_0\rangle = |\psi_{L\times N}\rangle = 0$. Figure 2.4(a) shows the corresponding band structure of Fig. 2.2(a) with $N = 20$. Compared to Fig. 2.2(a), the bulk energy spectrum is connected by the edge modes.

The Chern numbers calculated from the bulk correspond to the pumped charge by the edge states. Let us consider the case where the Fermi energy lies at $E_F = 1$ in the second gap. If we tune the φ from 0 to 2π, the left-edge state suddenly emerges at φ_1 and gradually invades into the bulk. On the other hand, the right-edge state continuously leaves bulk and abruptly disappears at φ_2. The shift of the edge states changes the polarization of the system. Fig. 2.2(b) shows the polarization for φ. The discrete jumps of the polarization imply the

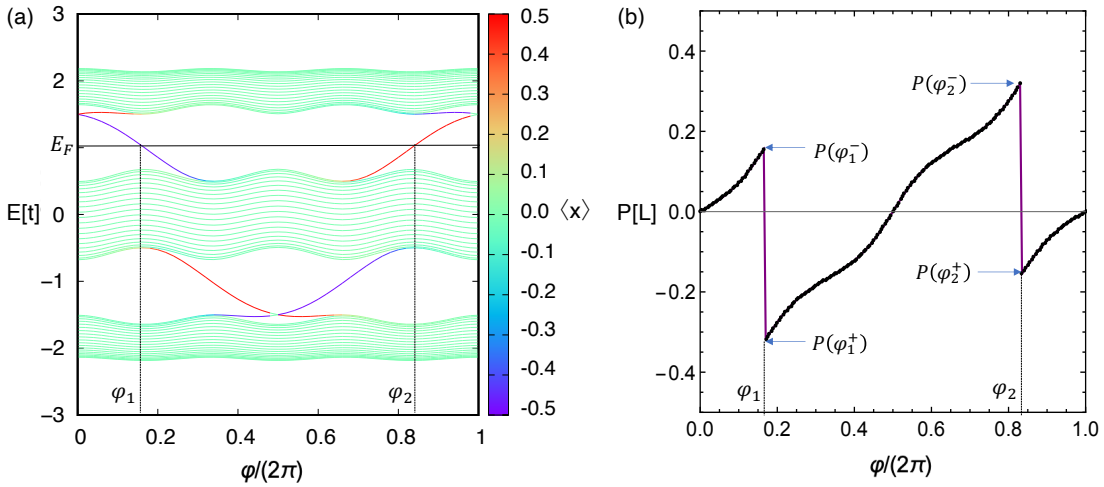

Figure 2.4: (a)Corresponding band structure of Fig. 2.2 with $N = 20$. The color label represents the expectation value of the position operator. (b)The time dependence of the polarization.

sudden occupation or unoccupation of the edge states at φ_1 and φ_2. Concretely, the electron localized at the left edge hosting $\langle x \rangle = -0.5$ disappears at φ_1. The number of pumped electrons is $C = \oint \mathrm{d}\varphi \partial_\varphi P/(eL)$ so that it can be rewritten as

$$C = \frac{1}{eL}\sum_i \left[P\left(\varphi_{i+1}^-\right) - P\left(\varphi_i^+\right)\right] = -\frac{1}{eL}\sum_i \left[P\left(\varphi_i^+\right) - P\left(\varphi_i^-\right)\right]. \qquad (2.35)$$

The first equation means that the number of pumped charges is equal to the sum of the continuous line of Fig. 2.2. The second equation indicates that it is also described by the opposite sign of the sum of the jump. This equation leads to $C = 1$, corresponding to the calculation from Eq.(2.20).

Although we discussed bulk-edge correspondence by using the specific model, the concept can be applied to any topological pumping. In Fig 2.5, we show the relation of the tangent of the edge state and its shift of polarization.

2.2 Twisted bilayer graphene

Here, we introduce the atomic and electronic structure of the twisted bilayer graphene. Weak van der Waals interlayer interactions enable us to stack bilayer graphene with an arbitrary twisted angle which leads to a long-range moire pat-

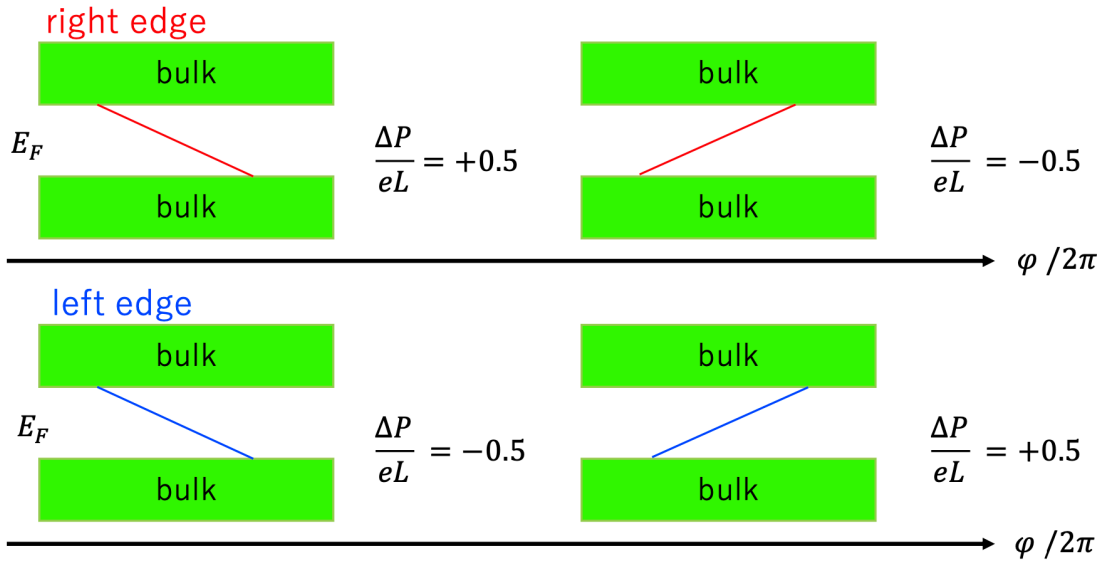

Figure 2.5: The dispersion of the edge state and the localization position determine the discontinuous jump of polarization.

tern with a period much greater than the atomic scale, called the moiré pattern. By applying a tight-binding approach, we show that the twist angle tunes the electronic structure and induces an isolated flat band at the magic angle.

2.2.1 Atomic structure

Figure 2.6 illustrates the atomic structure of TBG of 21.8°, 5.09° and 11.0°. The period of moiré superlattice is given by

$$L_M = \frac{a}{2\sin(\theta/2)} \tag{2.36}$$

where $a = 0.246$ nm is graphene's lattice constant. In $\theta \ll 1$, the moiré period can be approximated as $L_M \approx a/\theta$ and anti-proportional to the twisted angle. At the magic angle, L_M becomes around 14 nm, and the superlattice includes over ten thousand carbon atoms. Considering a TBG with a small rotation angle as in Fig. 2.6, we notice that the lattice structure locally resembles regular stacking such as AA, AB, BA, depending on the position. Here AA represents the perfect overlapping of hexagons, while AB and BA are shifted configurations in which the A(B) sublattice is right above B(A).

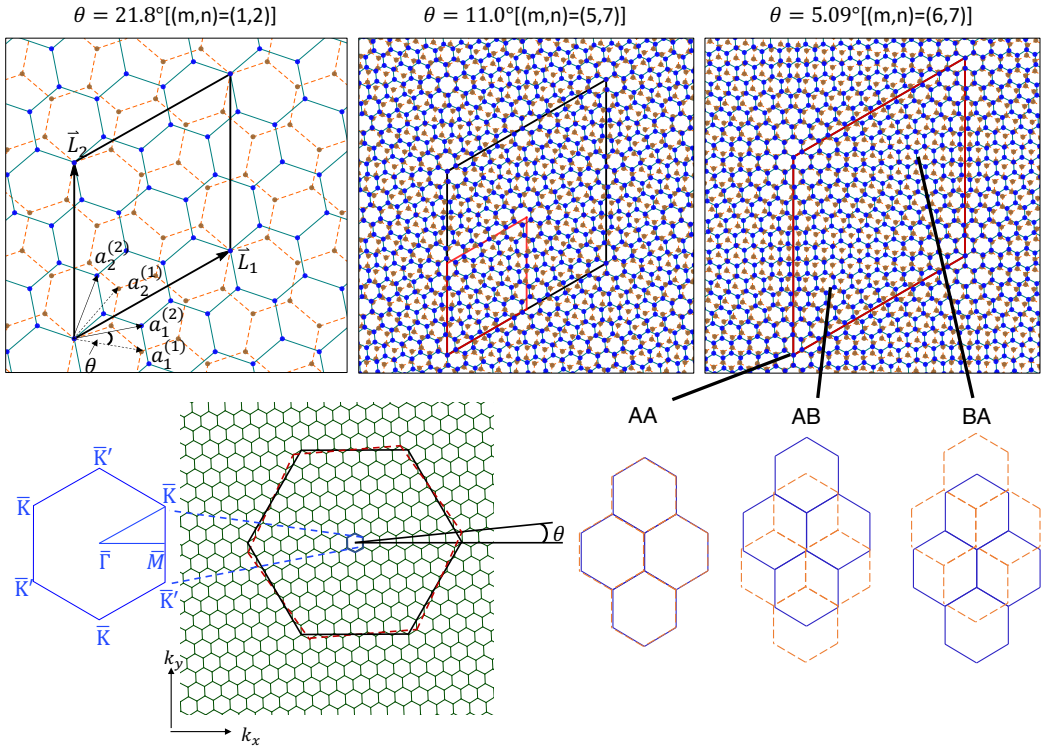

Figure 2.6: Atomic structures and the moiré unit cell of TBG with $\theta = 21.8°$, 5.09° and 2.65°. The inset shows the primitive lattice vectors of layers 1 and 2.

TBG can be generated from AA-stacked bilayer graphene (i.e., perfectly overlapping honeycomb lattices) by rotating layer 1 and 2 by $-\theta/2$ and $\theta/2$, respectively. We define $\mathbf{a}_1 = a(1,0), \mathbf{a}_2 = a(1/2, \sqrt{3}/2)$ as the lattice vectors of monolayer graphene before the rotation, where $a = 0.246$nm is graphene's lattice constant. The corresponding reciprocal lattice vectors are $\mathbf{b}_1 = (2\pi/a)(1, -1/\sqrt{3})$ and $\mathbf{b}_2 = (2\pi/a)(0, 2/\sqrt{3})$. The lattice vectors of layer l after the rotation are given by $\mathbf{a}_i^{(l)} = R(\mp\theta/2)\mathbf{a}_i$ with $\mp$ for $l = 1, 2$ respectively, where $R(\theta)$ represents the rotation by θ on xy-plane. Likewise, the reciprocal lattice vectors become $\mathbf{b}_i^{(l)} = R(\mp\theta/2)\mathbf{b}_i$. The Brillouin zones of layers 1 and 2 are shown in Fig. 2.6 by two large black, red dashed hexagons, respectively. In TBG, they are folded into reduced Brillouin zones, shown by small green hexagons. We label the corner points of the folded Brillouin zone by $\bar{K}$ and $\bar{K}'$, the midpoint of each side by $\bar{M}$, and the zone center by $\bar{\Gamma}$.

When the rotation angle is small, the mismatch of the lattice periods of two rotated layers gives rise to the long-period moiré pattern, of which the spatial period is estimated as follows. Suppose that in the rotation from the AA stacking, an atom on layer 1 and 2, originally located at site $\boldsymbol{r}_0$. The rotation moves the atoms into $\boldsymbol{r}_l = R(\pm\theta/2)\boldsymbol{r}_0$. Then we define the interlayer atomic shift $\delta(r)$ as the difference of the two atoms after the rotation,

$$\delta(\boldsymbol{r}_2) = \boldsymbol{r}_2 - \boldsymbol{r}_1 = \left(1 - R^{-1}\right)\boldsymbol{r}_2 \tag{2.37}$$

When $\delta(\boldsymbol{r}_2)$ coincides with a lattice vector of layer 1, the atom of layer 2 at $\boldsymbol{r}_2$ is arranged on the above of an atom of layer 1. Therefore, the primitive lattice vector of the moiré superlattice L_i^M is obtained from the condition $\delta(\boldsymbol{L}_i^M) = \boldsymbol{a}_i^{(1)}$, which leads to,[12]

$$\begin{aligned}\boldsymbol{L}_i^M &= [R(\theta/2) - R(-\theta/2)]^{-1}\mathbf{a}_i \quad (i = 1, 2) \\ &= \frac{1}{2\sin(\theta/2)} R(-\pi/2)\mathbf{a}_i,\end{aligned} \tag{2.38}$$

The corresponding moiré reciprocal lattice vectors satisfying $\mathbf{G}_i^{\mathrm{M}} \cdot \mathbf{L}_j^{\mathrm{M}} = 2\pi\delta_{ij}$ are written as

$$\mathbf{G}_i^{\mathrm{M}} = [R(\theta/2) - R(-\theta/2)]\mathbf{b}_i = \mathbf{b}_i^{(1)} - \mathbf{b}_i^{(2)} \quad (i = 1, 2) \tag{2.39}$$

The atomic structure of TBG is not exactly periodic in general because the moiré period is generally incommensurate with the underlying atomic lattice. A commensurate structure with an exact period takes place when the twist angle θ coincides with the angle between $\mathbf{v}_1 = m\mathbf{a}_1 + n\mathbf{a}_2$ and $\mathbf{v}_2 = n\mathbf{a}_1 + m\mathbf{a}_2$ with certain integers m and n. Then the lattice points $\mathbf{v}_1$ on layer 1 and $\mathbf{v}_2$ on layer 2 of the non-rotated bilayer graphene merge after the rotation and a rigorously periodic structure is obtained. A lattice vector of the superlattice unit cell is then given by $\mathbf{L} = m\mathbf{a}_1^{(1)} + n\mathbf{a}_2^{(1)} = n\mathbf{a}_1^{(2)} + m\mathbf{a}_2^{(2)}$. The twist angle θ is equal to the angle between

$\mathbf{v}_1$ and $\mathbf{v}_2$, which is $\cos\theta = (1/2)(m^2+n^2+4mn)/(m^2+n^2+mn)$. The 60° rotation of $\mathbf{L}$ also gives a lattice vector because of C_6 rotational symmetry. We can choose two primitive lattice vectors as $\boldsymbol{L}_1 = R(-2\pi/3)\boldsymbol{L}$ and $\boldsymbol{L}_2 = R(-\pi/3)\boldsymbol{L}$, which can be written as

$$\begin{aligned}\mathbf{L}_1 &= n\mathbf{a}_1^{(1)} - (m+n)\mathbf{a}_2^{(1)} = m\mathbf{a}_1^{(2)} - (m+n)\mathbf{a}_2^{(2)} \\ \mathbf{L}_2 &= (m+n)\mathbf{a}_1^{(1)} - m\mathbf{a}_2^{(1)} = (m+n)\mathbf{a}_1^{(2)} - n\mathbf{a}_2^{(2)}.\end{aligned} \tag{2.40}$$

In this choice, the rigorous period and the moiré period are simply related by $\mathbf{L}_i = |m-n|\mathbf{L}_i^M$.[12]

2.2.2 Tight-binding model

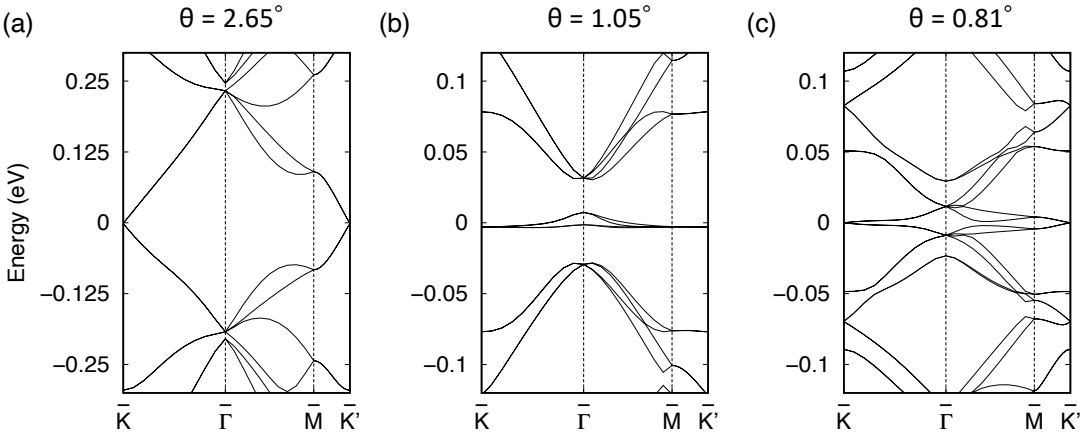

Figure 2.7: Band structure at various rotation angles for (a)$\theta = 2.65°$, (b)1.05° and (c)0.81°.

Here, we introduce the electric structure of TBG by using the tight-binding model for carbon p_z orbitals. The Hamiltonian is written as [3, 132, 133, 134]

$$H = -\sum_{\langle i,j\rangle} t\left(\mathbf{R}_i - \mathbf{R}_j\right)\left|\mathbf{R}_i\right\rangle\left\langle\mathbf{R}_j\right| + \text{H.c.} \tag{2.41}$$

where $\mathbf{R}_i$ and $|\mathbf{R}_i\rangle$ represent the lattice point and the atomic state at site i, respectively, and $t\left(\mathbf{R}_i - \mathbf{R}_j\right)$ is the transfer integral between site i and site j. We

adopt the Slater-Koster-type formula for the transfer integral,

$$\begin{aligned} -t(\mathbf{d}) &= V_{pp\pi}\left[1-\left(\frac{\mathbf{d}\cdot\mathbf{e}_z}{d}\right)^2\right]+V_{pp\sigma}\left(\frac{\mathbf{d}\cdot\mathbf{e}_z}{d}\right)^2 \\ V_{pp\pi} &= V^0_{pp\pi}\exp\left(-\frac{d-a_0}{\delta_0}\right) \\ V_{pp\sigma} &= V^0_{pp\sigma}\exp\left(-\frac{d-d_0}{\delta_0}\right) \end{aligned} \quad , \tag{2.42}$$

where $\mathbf{d}=\mathbf{R}_i-\mathbf{R}_j$ is the distance between two atoms, and $\mathbf{e}_z$ is the unit vector on the z axis. $V^0_{pp\pi}$ is the transfer integral between the nearest-neighbor atoms of monolayer graphene, which are located at a distance $a_0=a/\sqrt{3}\approx 0.142$ nm. $V^0_{pp\sigma}$ is the transfer integral between the two nearest vertically aligned atoms, $d_0\approx 0.335$nm is the interlayer spacing. δ_0 is the decay length of the transfer integral and is chosen as $0.184a$. The transfer integral for $d>\sqrt{3}a$ is exponentially small and can be safely neglected.

In Fig. 2.6, we are supposed that the two graphene layers are rigid and simply stacked without reconstruction of honeycomb lattices. However, in a real system, the lattice structure spontaneously deforms to obtain an energetically stable configuration[135, 136, 137, 138, 139, 140], and it should influence the electronic spectrum. Because the interlayer binding energy is the lowest in AB and BA and the highest in AA stacking region[135, 141, 142, 140], the TBG spontaneously relaxes in the plane for maximizing the AB/BA areas and minimizing the AA area. In fact, the AB/BA domain structure was experimentally observed [143, 144, 145]. The in-plane lattice relaxation in the TBG atomic structure gives an energy gap between the flat bands and the excited bands. There is another lattice reconstruction caused by out-plane relaxation. In this thesis, we neglect the effect because it just enhances the moiré gap, which is obtained by including the in-plain relaxation.

In Fig. 2.7, we show the calculating band structure from Eq. (2.41) at (a) $\theta=2.65°$, (b) $1.05°$ and (c) $0.81°$. The energy crossing of Dirac cones from each layer is gapped out, and the ratio of the width and Dirac dispersion be-

comes larger in decreasing twisted angle. Especially at $\theta = 1.05°$, the band dispersion of the Dirac cone vanishes, and the gap between the flat and excited band is around 25meV.[140] The flat band has a significant role in the strongly correlated effect, such as superconductivity and correlated insulating phase.[13, 16, 14, 15] The dispersion is recovered by decreasing the twist angle from the magic angle. Moreover, the wavefunction of the flat band well localizes at the AA spot [Fig.2.9] because the area has stronger interlayer coupling compared to the AB/BA regions.[4, 5, 7, 11] Note that the TBG of $\theta = 2.65°$, $1.05°$ and $0.81°$. is a commensurate system at which the atomic structure is exactly periodic in the moiré period $\mathbf{L}_i^M$ [1, 7, 6, 12, 9, 146, 147, 148], and hence the eigenstates of the tight-binding model can be obtained by diagonalizing a finite-sized Hamiltonian matrix.

The magic angle TBG contains a huge number of atoms (about 12,000) in the moiré unit cell [Fig. 2.8(a)], requiring a large computational cost to calculate the energy bands. Here, we explain a method to obtain the same eigenenergy of the magic angle TBG by using a smaller number of the carbon p_z orbitals. To reduce the number of atoms, we can take the atomic structure of $\theta = 2.65°$ which has 10 times fewer atoms per unit cell [Fig. 2.8(b)], but at the same time, enlarge the interlayer hopping energy (i.e., transfer integral between atoms of layer 1 and layer 2) by a factor of $2.65°/1.05° \approx 2.52$, to mimic the band structure of $\theta = 1.05°$ as shown in Figs. 2.8(c) and (d). The approximation works for the following reason. The low-energy band structure of TBG is determined by the ratio of two energy scales, t_{inter}/E_M, where t_{inter} is the interlayer hopping energy, and $E_M = \hbar v(2\pi/L_M) \sim (2\pi\hbar v/a)\theta$ is the moiré band folding energy with graphene's band velocity v.[1, 7, 6, 12, 9, 146, 147, 148] Therefore, the TBG of $\theta = 2.65°$ with t_{inter} multiplied by factor 2.52 has a nearly identical low-energy band structure as the original $\theta \sim 1.05°$ model except for the overall energy scale. It is worth noting that this approximation is based on the effective continuum model developed by [1, 7, 6, 12, 9, 146, 147, 148]. The effective model can accurately reproduce the

energy spectrum of the tight-binding model only in the low twist angle regime. Thus, the method is not applicable if the tight-binding model of a large twist angle ($> 3°$) is used to calculate the band structure of the magic angle TBG. Also, we include the in-plane lattice relaxation in the TBG atomic structure. Here we set the lattice displacement vector $\mathbf{u}$ of $\theta = 1.05°$ [140] in the lattice of 2.65° TBG, and construct the tight-binding Hamiltonian. Figure 2.8(f) plots the bulk band structure calculated for the 2.65° model with three-times enlarged interlayer hopping, showing a quantitative agreement to that of the magic angle TBG [Fig. 2.8(e)] except for the energy scale difference by the factor about 2.52.

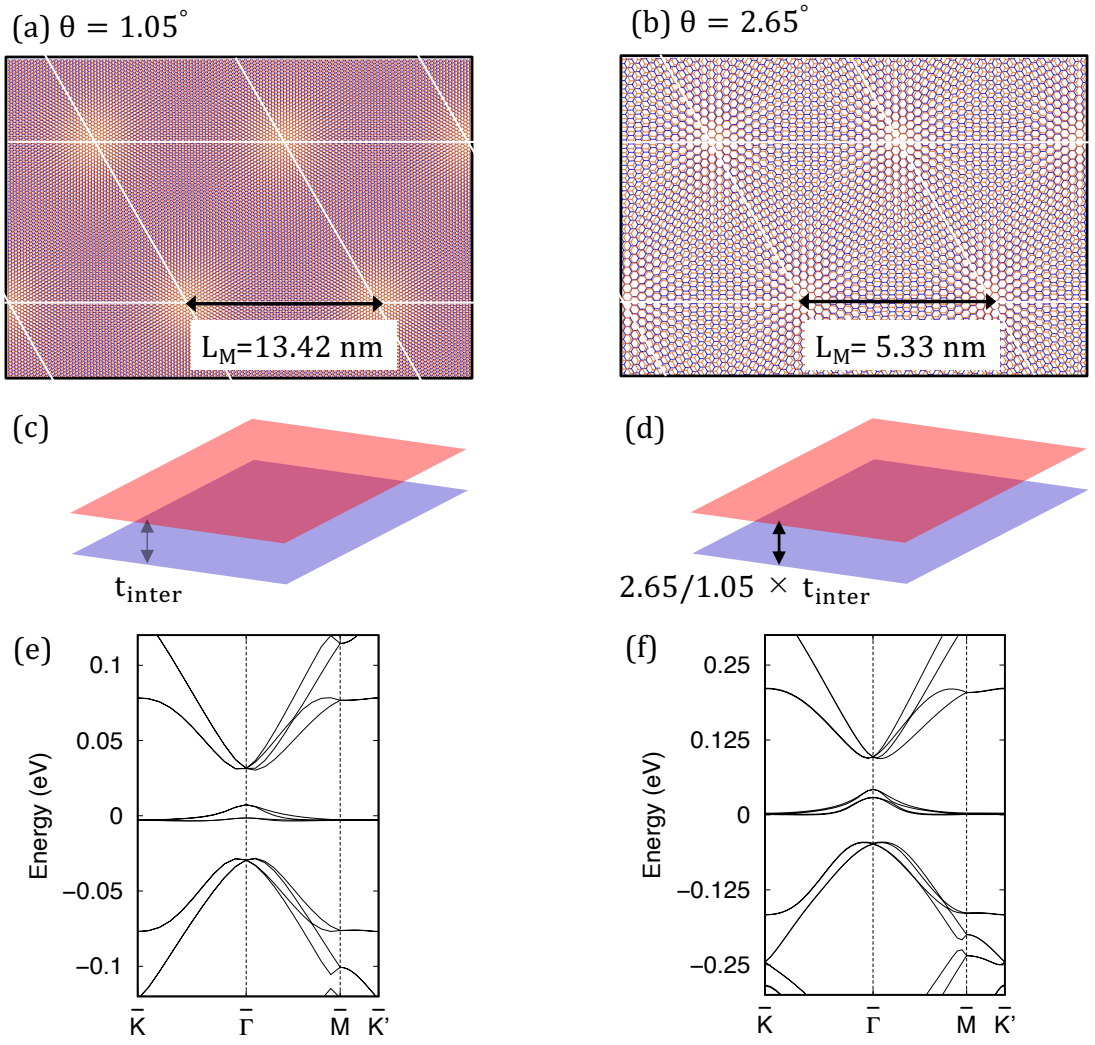

Figure 2.8: The lattice structure of TBG for (a)1.05° and (b)$\theta = 2.65°$. (c) and (d) are the schematic pictures of changing the interlayer coupling for reproducing the energy spectrum of (a)1.05° by using the tight-binding model of (b)2.65°. We enlarge the interlayer hopping t_{inter} by factor 2.65/1.05. This corresponds to tuning the length of moiré superlattice (b) into that of (a). (e)The Band structure of 1.05° is similar to (f)that of $\theta = 2.65°$ tight-binding model with enlarged interlayer hopping by factor 2.52.

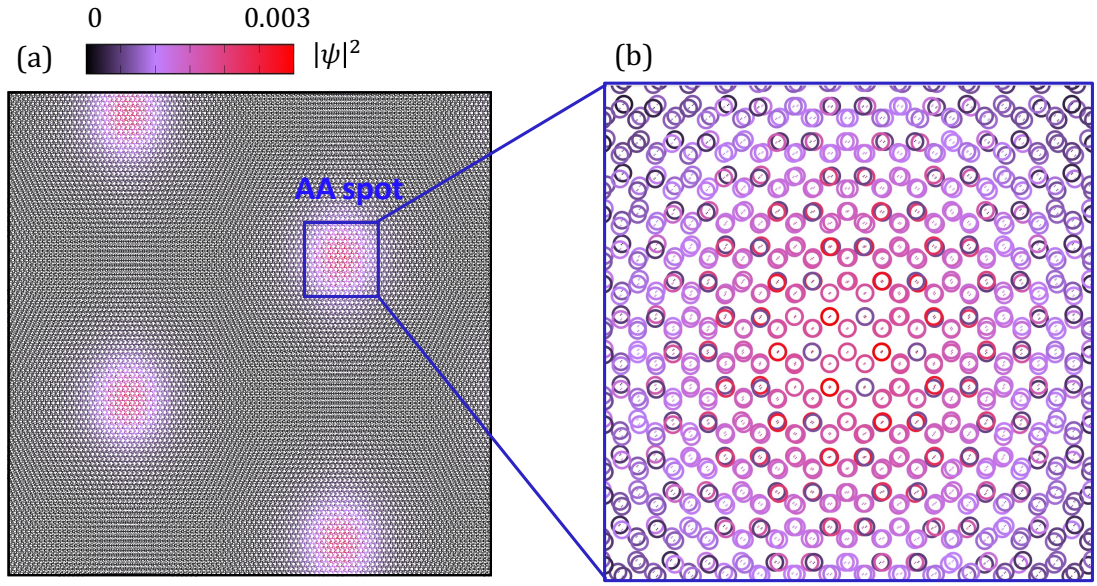

Figure 2.9: (a)The wavefunction of the flat band of the magic angle TBG. (b) the expansion of Figure (a) around the AA spot

Chapter 3

Topological charge pumping by a sliding moiré pattern

In this Chapter, we study the topological charge pumping driven by interlayer sliding in the moiré superlattices. We first consider a one-dimensional (1D) double-chain model composed of two tight-binding chains with different lattice constants. We show that the number of pumped charges in the interlayer sliding process is quantized into a sliding Chern number, which satisfies a Diophantine equation similar to that for the quantum Hall effect. Second, we apply the same argument to TBG and find that eight Chern numbers are associated with every single gap. In low-angle TBG, we show that the moiré gaps have non-zero sliding Chern numbers. When the Fermi energy is in either of those gaps, the electrons follow the movement of the moiré pattern.

3.1 Charge pumping in double chain model

Let us consider a 1D double chain as illustrated Fig. 3.1(a). The system contains two atomic chains with different lattice constants, which are arranged parallel to one another in a certain distance d_0. The chains are denoted by 1 and 2 and their lattice constants by a_1,a_2, respectively. In the following, we consider a commensurate case $N_1 a_1 = N_2 a_2 = L$ with integers N_1 and N_2, where a vertical overlap of an atom pair from both chains appears in a period L.

We calculate the eigenenergies and eigenfunctions in a double-chain tight-binding model with s atomic orbitals on every single site. The Hamiltonian is

written as

$$H = -\sum_{\langle i,j \rangle} t\left(\mathbf{R}_i - \mathbf{R}_j\right) \left|\mathbf{R}_i\right\rangle \left\langle \mathbf{R}_j\right| + \text{H.c.} \tag{3.1}$$

where $\mathbf{R}_i$ and $|\mathbf{R}_i\rangle$ represent the lattice point and the atomic state at site i respectively, and $t\left(\mathbf{R}_i - \mathbf{R}_j\right)$ is the transfer integral between site i and site j. For the intra-chain hopping, we just take the nearest neighbor hopping and it is assumed to be the same for both chains and defined as a unit of energy. For the hopping between sites on the different chains, we assume $t(d) = t_0 e^{-(d-d_0)/\delta_0}$ where $d = |\boldsymbol{R}_i - \boldsymbol{R}_j|$ and δ_0 is decay length. In this paper, we assume $t_0 = 4.0, d_0 = 1.0$ and $\delta_0 = 0.1$.

We consider an adiabatic charge pumping caused by a relative sliding of chains. By starting from an initial state in Fig. 3.1(a), we horizontally shift either of chain $l = 1$ or 2 by λa_l $(0 \leq \lambda \leq 1)$ with the other chain fixed. When λ is increased from 0 to 1, the Hamiltonian returns to its original state. We assume that the shift occurs in a sufficiently long time so that we can treat the problem as an adiabatic topological pumping [89]. The charge transport in such a process is expressed as a change of the polarization. If the Fermi energy lies inside a certain gap of the spectrum, the electric polarization, or the center of mass of the occupied electrons, is given by

$$P(\lambda) = \sum_{n \in \text{occ.}} \frac{L}{2\pi} \int_{-\frac{\pi}{L}}^{\frac{\pi}{L}} dk \; i\langle u_{nk}(\lambda)| \frac{\partial}{\partial k} |u_{nk}(\lambda)\rangle \tag{3.2}$$

where $u_{nk}(\lambda)$ is the Bloch eigenstate of the nth band in the instantaneous Hamiltonian at shift λ, and occ. represents the occupied bands below the Fermi energy. The charge transport during the process is then given by $\Delta P = \int_0^1 d\lambda (\partial P/\partial \lambda)$. This is expressed as $\Delta P = CL$ with the sliding Chern number,

$$C = \sum_{n \in \text{occ.}} \frac{iL}{2\pi} \int_{-\frac{\pi}{L}}^{\frac{\pi}{L}} dk \int_0^1 d\lambda \left[\left\langle \frac{\partial u}{\partial \lambda} \middle| \frac{\partial u}{\partial k} \right\rangle - \left\langle \frac{\partial u}{\partial k} \middle| \frac{\partial u}{\partial \lambda} \right\rangle \right], \tag{3.3}$$

where $u = u_{nk}(\lambda)$. We can define two different Chern numbers C_l $(l = 1, 2)$ for

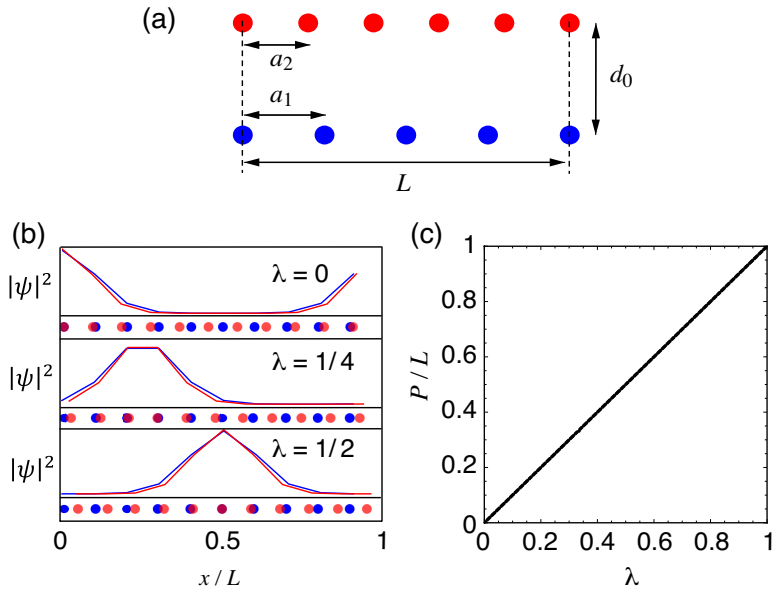

Figure 3.1: (a) Double chain model with $N_1 = 4, N_2 = 5$. (b) Evolution of a wave function of the lowest band in the double chain of $(N_1, N_2) = (10, 11)$, where the chain 2 (red) is shifted by λa_2 with the chain 1 (blue) fixed. (c) Polarization P [Eq. (3.2)] in the lowest gap as a function of sliding parameter λ.

the movement of chain l.

Fig. 3.1(b) shows the evolution of a wave function of the lowest band in the double chain of $(N_1, N_2) = (10, 11)$, where the chain 2 (red) is shifted by λa_2 with the chain 1 (blue) fixed. The blue and red dots in the bottom represent the horizontal positions of chain 1 and 2, respectively. We see that the wave center exactly follows the atom overlap region, i.e., the region where the chain 1 atoms and chain 2 atoms are overlapping in the horizontal position. In this particular system $(N_2 - N_1 = 1)$, the center of the overlap region is given by at $x = \lambda L$ as a function of sliding parameter λ, so it moves exactly by the superlattice period L from $\lambda = 0$ to 1. In Fig. 3.1(c), we plot the polarization P [Eq. (3.2)] in the lowest gap as a function of shift λ, where we actually see that the charge is pumped by L after one cycle, i.e. $C_2 = 1$. We can consider a similar process to move chain 1 by fixing chain 2 instead, and then we have $C_1 = -1$, i.e. the change is pumped by a single moiré period in the negative direction.

We calculate the band structure and the sliding Chern numbers for various configurations of N_1 and N_2. In Fig. 3.2, we plot the energy spectrum as a

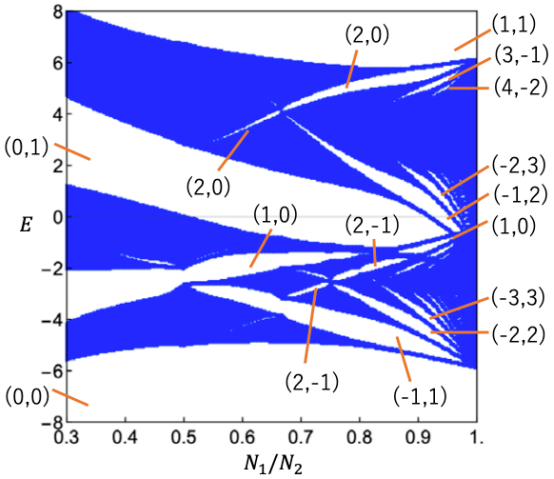

Figure 3.2: Energy spectrum of the one-dimensional double chain model as a function of N_1/N_2. The numbers assigned to gaps indicate the sliding Chern numbers (C_1, C_2).

function of N_1/N_2, where the filled area represents the energy region where the eigenstates exist, and the numbers assigned to the gaps are the sliding Chern numbers (C_1, C_2). The picture shows some similarities with Hofstadter's butterfly [128] with the quantized Hall integers in two-dimensional periodic system under the magnetic field[100]. Actually, the sliding Chern numbers can be found by using a Diophantine equation similar to that in the quantum Hall systems[100], without integrating the Berry curvature in Eq. (3.3), as in the following manner.

Let us consider a double chain specified by N_1 and N_2, and assume the Fermi energy lies in a gap with r bands below, i.e., r bands out of $N_1 + N_2$ bands in total are fully occupied. If we fix chain 2 and shift chain 1 by $L(= N_1 a_1)$, the number of pumped electrons is given by $N_1 C_1$ i.e., $N_1 C_1$ electrons passed through any cross-section perpendicular to the double chain. On the other hand, if we fix chain 1 and shift chain 2 by $-L(= -N_2 a_2)$, the number of pumped electrons is given by $-N_2 C_2$, i.e., $N_2 C_2$ electrons passed in the negative direction. The former and the latter processes share the same relative motion between the two chains, but differ only in the absolute position of the final state by L. If we shift the whole system (chain 1 and 2 together) by L following the latter process, it causes a pump of extra r electrons, because the number of electrons per a superlattice

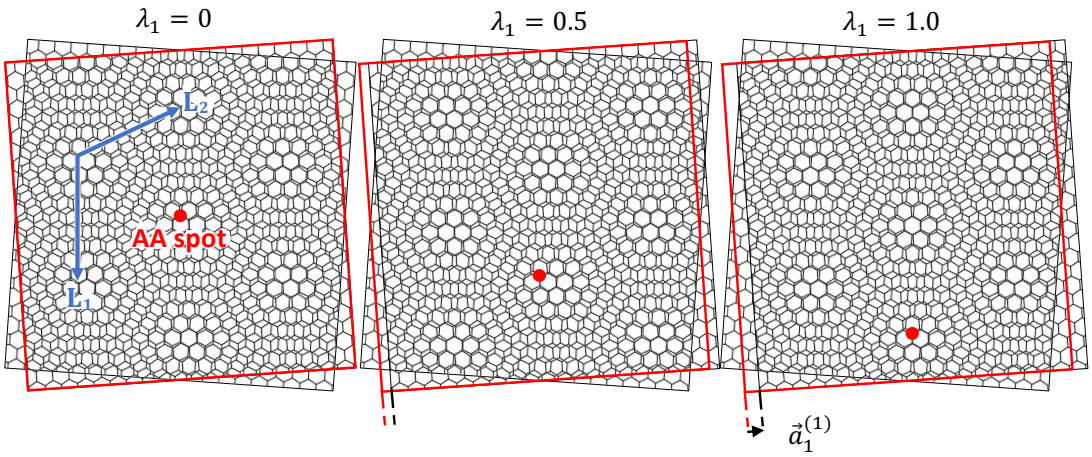

Figure 3.3: Moiré sliding in twisted bilayer graphene. We slide layer 1 by $\lambda = 0$(left), $lambda = 0.5$(middle) and $lambda = 1.0$ then the moiré pattern shifts λL_M. During this process, the AA spot represented by red dot moves by λL_M

period L is equal to the number of the occupied bands, r. The equality of the two processes leads to $N_1 C_1 = -N_2 C_2 + r$, or

$$N_1 C_1 + N_2 C_2 = r, \tag{3.4}$$

which is a Diophantine equation for the sliding Chern numbers.

If we define the ratio of the double periods as $\alpha = N_1/N_2 = a_2/a_1$ and the electron density as $\rho = r/N_2$, we have $\rho = C_1\alpha + C_2$. Now the Chern numbers C_1 and C_2 can easily be derived from the diagram of Fig. 3.2, by counting the number of states below a particular gap as a function of α, and calculating $\partial\rho/\partial\alpha$. This is an analog to the Středa's formula in the integer quantum Hall effect. [127]

3.2 Twisted bilayer graphene

Now let us consider the charge pumping of a commensurate TBG. We adiabatically slide the layer $l(= 1 \text{ or } 2)$ by its own lattice period $\mathbf{a}_i^{(l)}$ $(i = 1 \text{ or } 2)$ while the other layer is fixed. Figure 3.3 shows the sliding process for $\lambda_1 = 0 \to 1$. The moiré pattern then moves exactly by $\mathbf{L}_1$. The variation of polarization in this process is written as

$$\Delta \mathbf{P} = C_{i1}^{(l)} \mathbf{L}_1 + C_{i2}^{(l)} \mathbf{L}_2, \tag{3.5}$$

$$C_{ij}^{(l)} = \sum_{n=\text{occ.}} \frac{iS}{(2\pi)^2} \int_{\text{BZ}} d^2k \int_0^1 d\lambda_i \left[\left\langle \frac{\partial u}{\partial \lambda_i} \middle| \frac{\partial u}{\partial k_j} \right\rangle - \left\langle \frac{\partial u}{\partial k_j} \middle| \frac{\partial u}{\partial \lambda_i} \right\rangle \right] \tag{3.6}$$

where $u = u_{n\boldsymbol{k}}(\lambda_1, \lambda_2)$ is the Bloch eigenstate in the instantaneous Hamiltonian with the layer l shifted by $\lambda_1 \mathbf{a}_1^{(l)} + \lambda_2 \mathbf{a}_2^{(l)}$, BZ represents the first superlattice Brillouin zone, $S = |\mathbf{L}_1 \times \mathbf{L}_2|$ is the superlattice unit cell area. $\partial/\partial k_j = (\boldsymbol{G}_j/|\boldsymbol{G}_j|) \cdot \nabla_{\boldsymbol{k}}$, and $\mathbf{G}_j$ is the reciprocal lattice vectors satisfying $\mathbf{G}_i \cdot \mathbf{L}_j = 2\pi\delta_{ij}$. The sliding Chern number $C_{ij}^{(l)}$ represents the number of electrons passed through the unit-cell side perpendicular to $\boldsymbol{G}_j$ (i.e., the cross-section spanned by $\boldsymbol{L}_2$ for $j = 1$, and $\boldsymbol{L}_1$ for $j = 2$), during an adiabatic sliding of the layer l by $\mathbf{a}_i^{(l)}$. It is formally similar to, but different from the Chern number for the quantized Hall conductivity [100], as it is related to derivative in a mechanical interlayer shift.

To obtain the Diophantine equation for the sliding Chern numbers in the TBG, we follow the same steps as in 1D. We assume that the Fermi energy is in a gap and r bands are fully occupied. Considering that a shift of layer 1 by $\mathbf{L}_1 (= n\mathbf{a}_1^{(1)} - (m+n)\mathbf{a}_2^{(1)})$ is equivalent to a shift of layer 2 by $-\mathbf{L}_1 (= -m\mathbf{a}_1^{(2)} + (m+n)\mathbf{a}_2^{(2)})$ followed by a shift of whole system by $\mathbf{L}_1$, we obtain

$$\begin{aligned} nC_{11}^{(1)} + mC_{11}^{(2)} - (m+n)(C_{21}^{(1)} + C_{21}^{(2)}) &= r, \\ nC_{12}^{(1)} + mC_{12}^{(2)} - (m+n)(C_{22}^{(1)} + C_{22}^{(2)}) &= 0. \end{aligned} \tag{3.7}$$

A similar argument for the shift by $\mathbf{L}_2$ gives

$$\begin{aligned} (m+n)(C_{11}^{(1)} + C_{11}^{(2)}) - mC_{21}^{(1)} - nC_{21}^{(2)} &= 0, \\ (m+n)(C_{12}^{(1)} + C_{12}^{(2)}) - mC_{22}^{(1)} - nC_{22}^{(2)} &= r. \end{aligned} \tag{3.8}$$

The exact lattice commensurability is not actually important in low twist angles, where the physical property is approximately described by the continuum model, which is periodic in the moiré period $\boldsymbol{L}_j^M$.[1, 6, 7, 9, 12, 146, 147, 148]

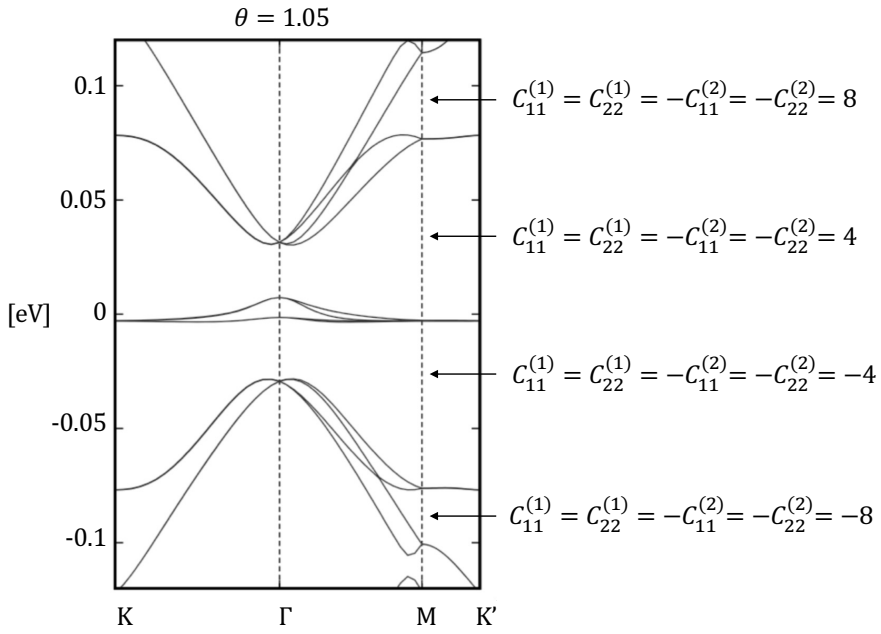

Figure 3.4: The numbers assigned to gaps indicate the sliding Chern numbers.

Indeed, Eqs. (3.7) and (3.8) can also be transformed in a continuous form as follows. Since the rigorous period $\boldsymbol{L}_j$ is $|m-n|$ times as large as the moiré period $\boldsymbol{L}_j^M$, a single continuum band corresponds to $|m-n|^2$ rigorous bands considering the zone folding, and therefore the number of occupied continuum bands is given by $\tilde{r} = r/|m-n|^2$. We can also define $\tilde{C}_{ij}^{(l)} = C_{ij}^{(l)}/|m-n|$ as the number of electrons passed through the cross-section spanned by $\boldsymbol{L}_j^M$ in the adiabatic sliding of the layer l by $\mathbf{a}_i^{(l)}$. Then Eqs. (3.7) and (3.8) become

$$\begin{aligned}
&\frac{\beta+1}{2}\tilde{C}_{11}^{(1)} + \frac{\beta-1}{2}\tilde{C}_{11}^{(2)} - \beta(\tilde{C}_{21}^{(1)} + \tilde{C}_{21}^{(2)}) = \tilde{r},\\
&\frac{\beta+1}{2}\tilde{C}_{12}^{(1)} + \frac{\beta-1}{2}\tilde{C}_{12}^{(2)} - \beta(\tilde{C}_{22}^{(1)} + \tilde{C}_{22}^{(2)}) = 0,\\
&\beta(\tilde{C}_{11}^{(1)} + \tilde{C}_{11}^{(2)}) - \frac{\beta-1}{2}\tilde{C}_{21}^{(1)} - \frac{\beta+1}{2}\tilde{C}_{21}^{(2)} = 0,\\
&\beta(\tilde{C}_{12}^{(1)} + \tilde{C}_{12}^{(2)}) - \frac{\beta-1}{2}\tilde{C}_{22}^{(1)} - \frac{\beta+1}{2}\tilde{C}_{22}^{(2)} = \tilde{r}.
\end{aligned} \tag{3.9}$$

where $\beta = (1/\sqrt{3})\cot(\theta/2)$. It is worth noting that in the low twist-angle regime, particularly, the sliding Chern number can be defined for each of nearly-decoupled K and K' valleys independently, and the number does not depend on the valley. Hence the total sliding Chern number is equal to twice that of a single valley.

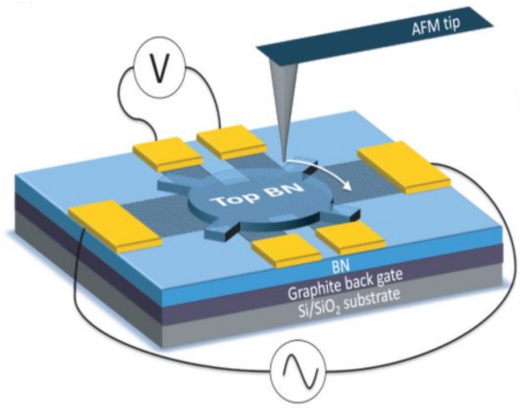

Figure 3.5: The mechanical translation of twisted bilayer graphene and graphene/BN heterostructures on h-BN substrate has been realized by using an atomic force microscope (AFM).[150]

This can be verified by considering the time-reversal symmetry in Eq.(3.6) (See, Appendix 6.1).

Figure 3.4 shows the calculated band structure for $1_0 5°$. The nearly-flat bands around the charge neutral point are separated from the rest of the spectrum by energy gaps. [149, 13, 16, 140, 46] If we assume that the Fermi energy lies in the gap just above the flat band, for example, we have $\tilde{r} = 4$ (relative to the charge neutral) by including the spin and valley degeneracies. The set of equations of Eq. (3.9) can be regarded as identities for a variable β, as it stands for any θ's in the low-angle regime. Then the Chern numbers are uniquely determined as $\tilde{C}_{11}^{(1)} = \tilde{C}_{22}^{(1)} = 4$, $\tilde{C}_{11}^{(2)} = \tilde{C}_{22}^{(2)} = -4$ and otherwise 0. Since Eq.(3.6) includes the momentum integration in only one direction, we can define the Chern number not only the first gap for but also for the second gap as shown in Fig.3.4. Actually, we can show that sliding the layer l by $\mathbf{a}_i^{(l)}$ leads to the moiré-pattern movement by $\pm\mathbf{L}_i^M$ with $\pm$ for $l = 1, 2$, respectively. The above solution of $\tilde{C}_{ij}^{(l)}$ means that four electrons trapped at each AA-stacking region precisely follow the movement of the moiré pattern, as naturally expected.

3.3 Experimental feasibility

Let us estimate the magnitude of slide-driven topological current in the magic angle TBG when four electrons are included in the moiré superlattice. The sliding speed is limited by the adiabatic condition: $\langle \dot{H} \rangle \ll \Delta^2/\hbar$ where $\Delta = 20\text{meV}$ is the band gap between the flat band and the excited band. When the upper graphene layer is slid with respect to the lower by a velocity v_g, the time derivative of the Hamiltonian is roughly estimated by $\langle \dot{H} \rangle \approx 2\pi t_{\text{inter}} v_g/a$, since the interlayer Hamiltonian at a fixed point changes by an energy scale of t_{inter} in a single adiabatic cycle of $\Delta t = a/v_g$. Thus, the maximum velocity of the interlayer sliding is

$$v_g \ll \frac{a\Delta^2}{2\pi\hbar t_{\text{inter}}} = 200\,\text{m/s}. \tag{3.10}$$

In order to calculate the adiabatic current, we assume $v_g = 2\,\mu\text{m/s}$, which is much smaller than the maximum value above. If the length of a TBG sample is $5\,\mu\text{m}$, we find that the current is approximately 2 pA. We expect that it may be observed by the source and drain electrodes appropriately attached and the interlayer sliding is experimentally feasible by using a mechanical device [150][Fig. 3.5].

Here, we propose a methodology for observing the pumping phenomenon through the sliding of the interface between two graphites. Several experiments [151, 152] have realized the motion while keeping a finite twist angle. As shown in Fig. 3.6, a tungsten microtip can be employed to move the upper graphite in various directions while keeping the lower graphite fixed. Moreover, the electric structure of the twisted interface of two graphites at $\theta = 1.05^\circ$ is predicted to host an energy gap.[153] Therefore, the topological current would be observed in the twisted interface of graphites.

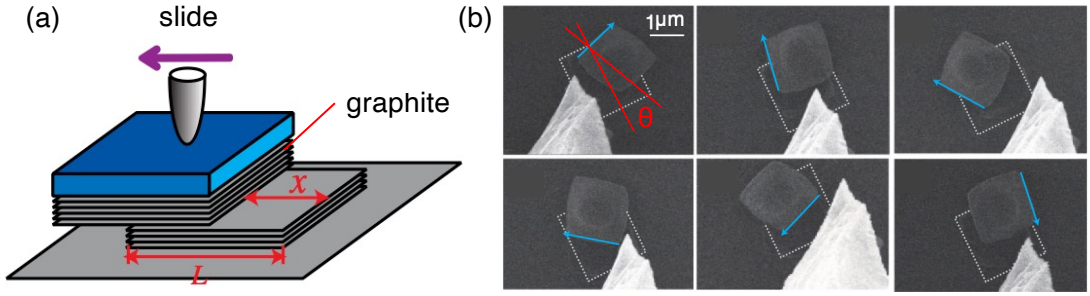

Figure 3.6: (a) Schematic illustration of sliding the upper graphite relative to the lower by using a microtip. The upper graphite is attached to the SiO_2 substrate. (b) The upper graphite is moved in various directions while keeping a twist angle relative to the lower graphite, as represented by the dashed square.[152]

Chapter 4

Bulk-edge correspondence of moiré pumping

In the previous chapter, we revealed that when one layer/chain of TBG/double chain is relatively slid with respect to the other layer by a single atomic period, then electrons are pumped by an integer multiple of the moiré period, where the integer is given by the sliding Chern number. One may ask if the new bulk topological numbers are related to edge states.

Here we investigate the edge states of the double chain model and TBG under the effect of the interlayer sliding. We calculate the finite models and demonstrate that the edge states are transferred in the energy axis during the interlayer sliding process. The number of edge states pumped in a sliding cycle equals the sliding Chern number of the band gap. The relationship can be viewed as a bulk-edge correspondence inherent in moiré bilayer systems.

4.1 Double chain model

Here, we investigate the edge states of the double chain model with adiabatic interlayer sliding. Let us consider the following atomic structure: a parallel alignment of a smaller length of tight-binding chain with fixed and a larger length of tight-binding chain l with slid by $\lambda a_l (0 \leq \lambda \leq 1)$. When λ is increased from 0 to 1, the Hamiltonian returns to its original state. For example, Fig.4.1(d) shows the case where the larger chain is chain 1 with shifted by $-\lambda a_1$. Chain 1 and chain 2 are commensurate with $(N_1, N_2) = (10, 11)$, the length of chain 1 is

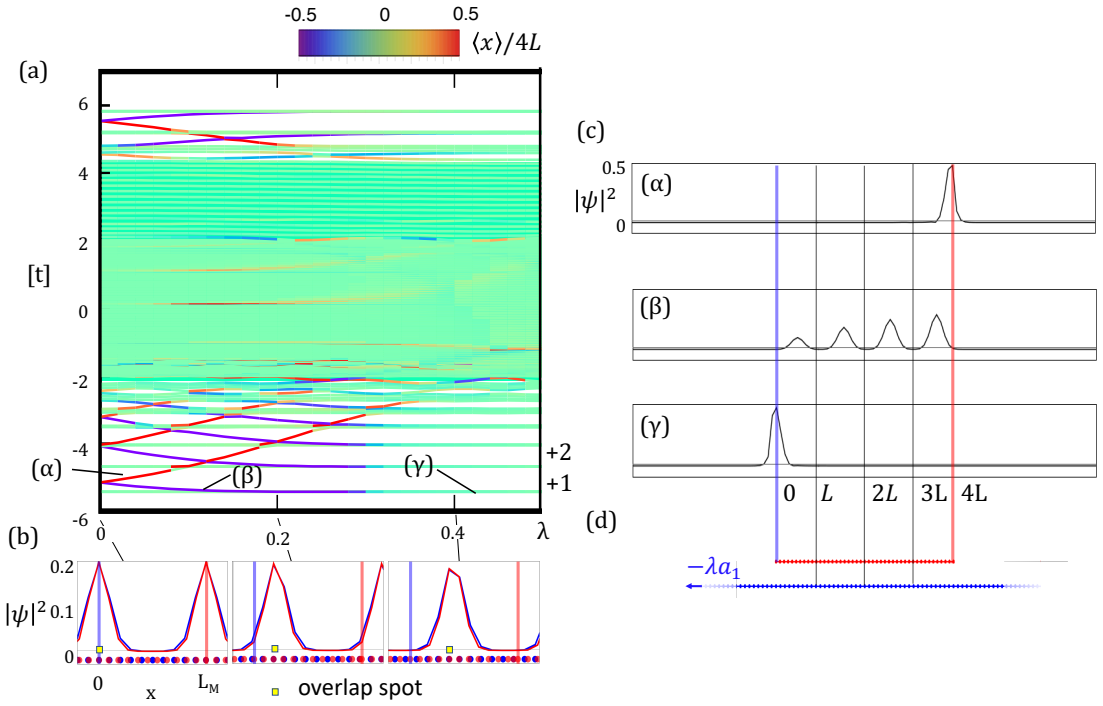

Figure 4.1: (a) Energy band structure of the island type of double chain model depicted in Fig.(d) as a function of sliding parameter λ ($0 \leq \lambda \leq 0.5$). (b) Real-space map of the lowest band's wave function at $k = 0$ of bulk double chain model at $\lambda = 0, 0.2, 0.4$. The red and blue vertical lines represent the boundary lines for the red chain. (c) Real-space map of eigenstates of the island type of double chain model. (α), (β) and (γ) are labelled in Fig. 4.4(a).

$20L(= 20 \times 10a_1)$ and the length of chain 2 is $4L(= 4 \times 11a_2)$, respectively. In the following, we consider the edge state for this model, named *island type of double chain model*.

The calculated energy spectrum shows in Fig. 4.1(a) that the green lines indicate the energy level localized in bulk, and the red/blue lines represent the energy level localized at the right/left edge. At $\lambda = 0$ and 1, we have a C_2 symmetry for the vertical plane of the chains, and there the edge states at left and right boundaries are forced to degenerate. In increasing λ from 0 to 0.5, we see that an edge band of the left boundary (blue lines) in the lowest gap is eventually absorbed into the lowest band. Because of the C_2 symmetry, the energy spectrum is mirror symmetric with respect to the $\lambda = 0.5$ axis, where the localized positions of the wavefunctions are opposite. Therefore, during λ from 0.5 to 1, an edge band of the right boundary (red lines) is released from the lowest band.

In Fig.4.1(b), we present the squared wave function of the lowest band (both chains are infinite) at $\lambda = 0, 0.2, 0.4$. The wave center exactly follows the atom overlap region λL (yellow dot), as shown in the previous chapter. The emergence of the edge states correlates with the relative position of the overlap region to the boundary lines. By comparing Figs. 4.1(a) and 4.1(b), we notice that the edge state of the left boundary (blue curves) located at the gaps of the electron side is absorbed into the lower band when the overlapped region enters the inside of the chain. Similarly, the edge state of the right boundary (red curves) which degenerates the blue energy at $\lambda = 0$, obtains higher energy with the sliding. They also branch out from each band when the overlapped region approaches the right boundary in the latter half of the process.

Figure 4.1(c) illustrates actual eigenstates of the island type of double chain model, (α), (β) and (γ) are labelled in Fig. 4.4(a). We see that the in-gap states (α) and (γ) are localized on the right edge and left edge, respectively, while the bulk state (β) extends over the middle region and the spatial oscillation follows

the moiré period.

The number of edge states branching out or being absorbed per a sliding cycle ($0 \leq \lambda \leq 1$) exactly coincides with the sliding Chern number, calculated in the previous chapter and written in the right row of Fig. 4.1(a) for the shift of chain 1 by $-a_1$. The figure also shows that, in the first/second gap, one band/two bands of the right edge states go up, and that of the left edge state goes down in one cycle. The corresponding sliding Chern number of the first gap is $-C_1 = +1$, and that of the second gap is $-C_1 = +2$. These numbers coincide with the number of transferred edge states across the gap, which can be viewed as a bulk-edge correspondence in the double-chain model. The coincidence can be seen not only electron side but also hole side, as shown in Fig. 4.1(a).

4.2 Model for twisted bilayer graphene

If we slide the layer l by $\mathbf{a}_i^{(l)}$ with the other layer fixed, the moiré pattern shifts exactly by $\pm\mathbf{L}_i^M$ for $l = 1, 2$, respectively. Therefore, when we slide the layer l by an arbitrary displacement vector,

$$\Delta\mathbf{x}^{(l)} = \nu_1\mathbf{a}_1^{(l)} + \nu_2\mathbf{a}_2^{(l)}, \tag{4.1}$$

then the moiré pattern moves by

$$\begin{aligned}\Delta\mathbf{X} &= \pm(\nu_1\mathbf{L}_1^M + \nu_2\mathbf{L}_2^M) \\ &= \frac{\pm 1}{2\sin(\theta/2)} R(-\pi/2 \mp \theta/2)\Delta\mathbf{x}^{(l)},\end{aligned} \tag{4.2}$$

where each double sign corresponds to $l = 1, 2$, respectively. When $\theta \ll 1$, the moiré pattern shift $\Delta\mathbf{X}$ is nearly perpendicular to the sliding vector $\Delta\mathbf{x}^{(l)}$, and its amplitude is magnified by the factor $[2\sin(\theta/2)]^{-1} \sim 1/\theta$.

In the following, we consider a TBG nanoribbon as shown in Fig. 4.2(a) to investigate the edge states. Note that the figure is rotated by 90° so that x axis

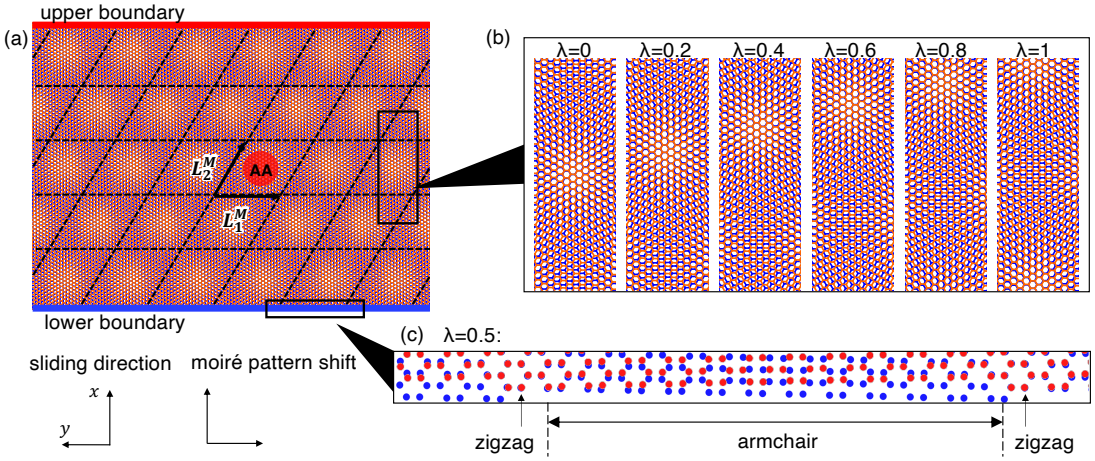

Figure 4.2: (a) TBG nanoribbon with 2.65° truncated by upper (red) and lower (blue) boundaries. Note that the figure is rotated by 90° so that x axis is vertical and y axis is horizontal. The structure is periodic in the direction of $\mathbf{L}_1^M$, and five unit cells thick in the perpendicular direction. (b) Detailed atomic structure in the sliding parameter $\lambda = 0, 0.2, ..., 1$. (c) The termination of the TBG nanoribbon for $\lambda = 0.5$. The boundary of each graphene is nearly the armchair edge, and the rest is the zigzag edge.

is vertical and y axis is horizontal. Here we assume that the ribbon is parallel to y and five unit cells thick in the perpendicular direction (along x), truncated by red and blue lines. As shown in Fig 4.2(c), the boundary is nearly parallel to the armchair direction of graphene so that the zigzag edge states of monolayer graphene are almost absent.

Now we slide layer 2 with respect to layer 1 along the length of the ribbon (y), to move the moiré pattern along the width (x). We specify the sliding vector by $(\nu_1, \nu_2) = \lambda(1/2, -1)\,(0 \leq \lambda \leq 1)$, which gives $\Delta\mathbf{x}^{(2)}$ almost along $-y$ direction. When the sliding parameter λ is changed from 0 to 1, the moiré pattern moves by $\Delta\mathbf{X} = -(1/2)\mathbf{L}_1^M + \mathbf{L}_2^M$ exactly in the x-direction. After the process, all the AA spots move just by one row, as illustrated in the lower panel of Fig. 4.2(b). Because of the triangular-lattice arrangement, the AA spots do not come back to the original positions, but as we will see, this process virtually gives a single cycle of the edge states pumping.

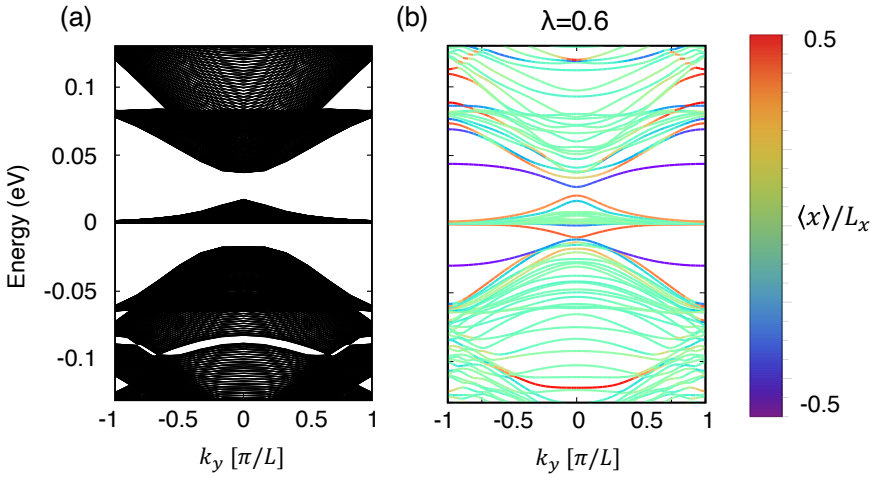

Figure 4.3: (a) The calculated band structure of the bulk TBG projected onto k_y axis. (b) The energy band structure of TBG nanoribbon against k_y at $\lambda = 0.6$. The colored lines depict the energy bands of the TBG ribbon, where the color represents the expected value of $\langle x \rangle / L_x$ coordinate where $L_x = 5L_M$.

4.3 Moiré edge state in twisted bilayer graphene

Here, we calculate the energy spectrum of the TBG by using the tight-binding model for $\theta = 2.65°$ with 2.52 times enlarged interlayer hopping, which is formulated in Sec.2.2.2. Figure 4.3(a) shows the energy bands of the bulk TBG projected onto k_y axis. In Fig. 4.3(b), we plot the energy spectrum of the TBG ribbon for $\lambda = 0.6$. The colored lines are the energy bands of the TBG ribbon, where the color represents the expected value of x coordinate; red (blue) lines indicate edge states localized at the upper (lower) boundary, while green lines are bulk states spreading over the entire system.

The dependence of the TBG ribbon's band diagram on the sliding parameter is summarized in Fig. 4.4. Here, Fig. 4.4(a) shows the band energies at the fixed wave number $k_y = \pi/L_1^M$, as a function of sliding parameter λ. Panel (b) presents the corresponding band structures of Fig. 4.3(b) at different sliding distances $\lambda = 0, 0.2, \cdots, 1$. The black-colored areas in the background correspond to Fig. 4.3(a). At $\lambda = 0$, we have an additional in-plane C_2 symmetry, which enforces the energetic degeneracy between the upper and lower edge states.

In increasing λ from 0 to 1, we see that two edge bands of the upper bound-

ary (red lines) split off from the zero-energy flat band in each of the positive and negative energy sides, and they are eventually absorbed into the excited conduction/valence bands. At the same time, two edge bands of the lower boundary (blue lines) transfer from the excited bands to the zero-energy band. The emergence of the edge states can be understood from the relative position of the wave function of the flat band and the boundaries, as follows.

In Fig. 4.4(c), we present the squared wave function of the flat band states at $\bar{K}$ of a bulk TBG (not of the ribbon) at $\lambda = 0, 0.2, \cdots, 1$. Here, the orange dots represent AA spots, and the red and blue lines represent the boundary lines for the ribbon. The wave amplitude is concentrated on the AA spots, which is a property of the flat band states [4, 5, 7, 11]. In increasing λ, the bright spots on the AA region shift upward to follow the moiré pattern movement. The emergence of the edge states correlates with the relative position of the AA spots to the boundary lines.[118] By comparing Figs. 4.4(a) and 4.4(c), we notice that two edge states of the top boundary (red curves) branch out from the zero-energy flat band when the AA spots cross the boundary to the outside, and similarly, the two edge states of the lower boundary (blue curves) are absorbed into the flat band when the AA spots enter the ribbon from the lower boundary.

Figure 4.5(b) illustrates the actual eigenstates of the TBG ribbon. We see that the in-gap states (1) and (2) are localized on the upper edge, and (5) and (6) are on the lower edge, while the bulk states (3) and (4) extend over the middle region. These edge states decay with the length of the moiré pattern, thus they are referred to as moiré edge states. [113, 114, 115, 116, 117, 118]

4.4 Bulk edge correspondence

The number of edge states branching out or being absorbed per a sliding cycle ($0 \leq \lambda \leq 1$) exactly coincides with the sliding Chern number, which is a topological invariant defined for the Bloch bands of TBG [154, 155, 156]. According to Sec.3.2, when the Fermi energy is in the gap just above the flat

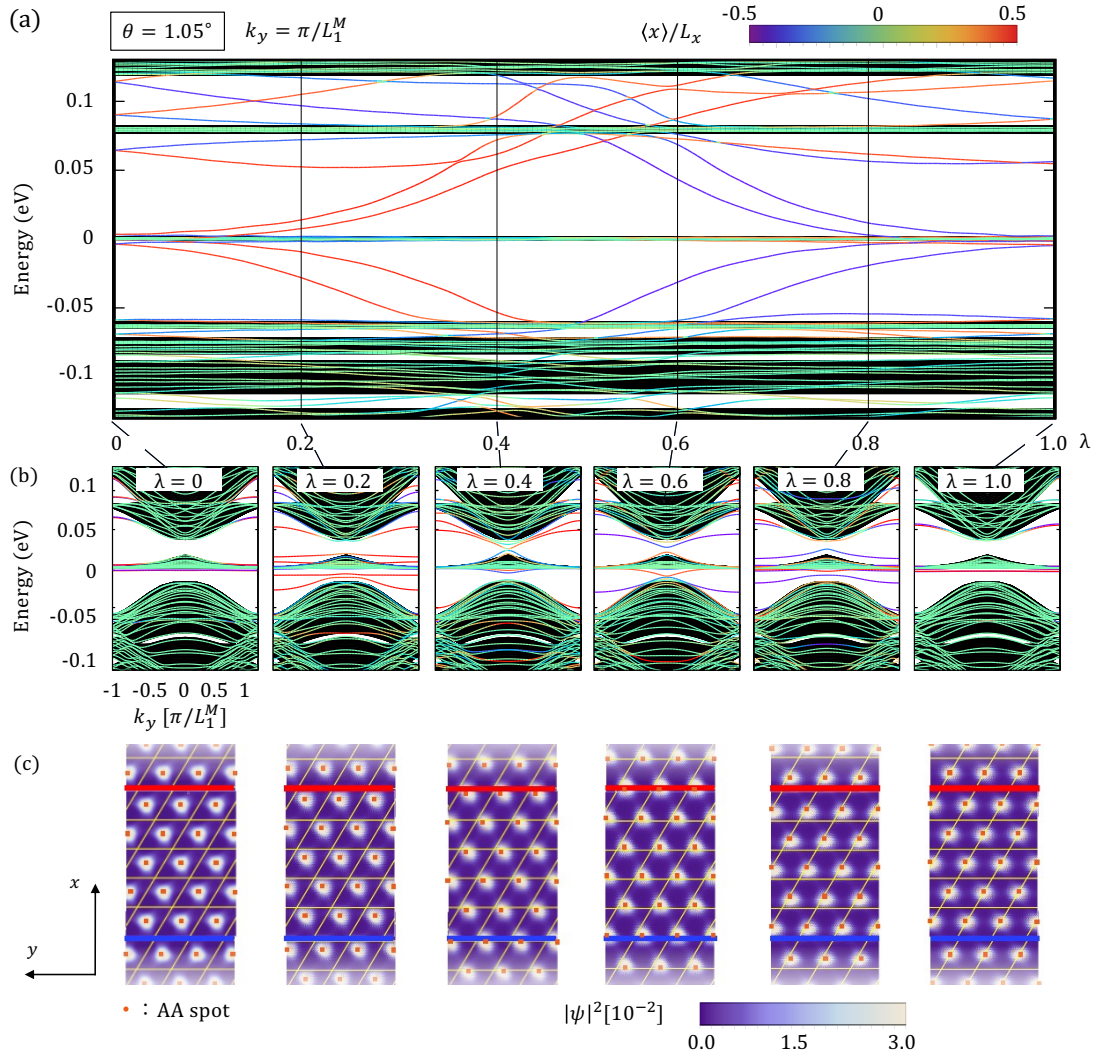

Figure 4.4: (a) Energy band structure of TBG nanoribbon at $k_y = \pi/L_1^M$ as a function of sliding parameter λ, and (b) the corresponding plot of Fig. 4.3(b) at $\lambda = 0, 0.2, \cdots, 1$. The area represented in black is identical to Fig. 4.3(a). (c) Real-space map of the flat-band wave function at $\bar{K}$ of bulk TBG at $\lambda = 0, 0.2, \cdots, 1$ [corresponding to upper panels in (b)]. The red and blue lines represent the boundary lines for the ribbon.

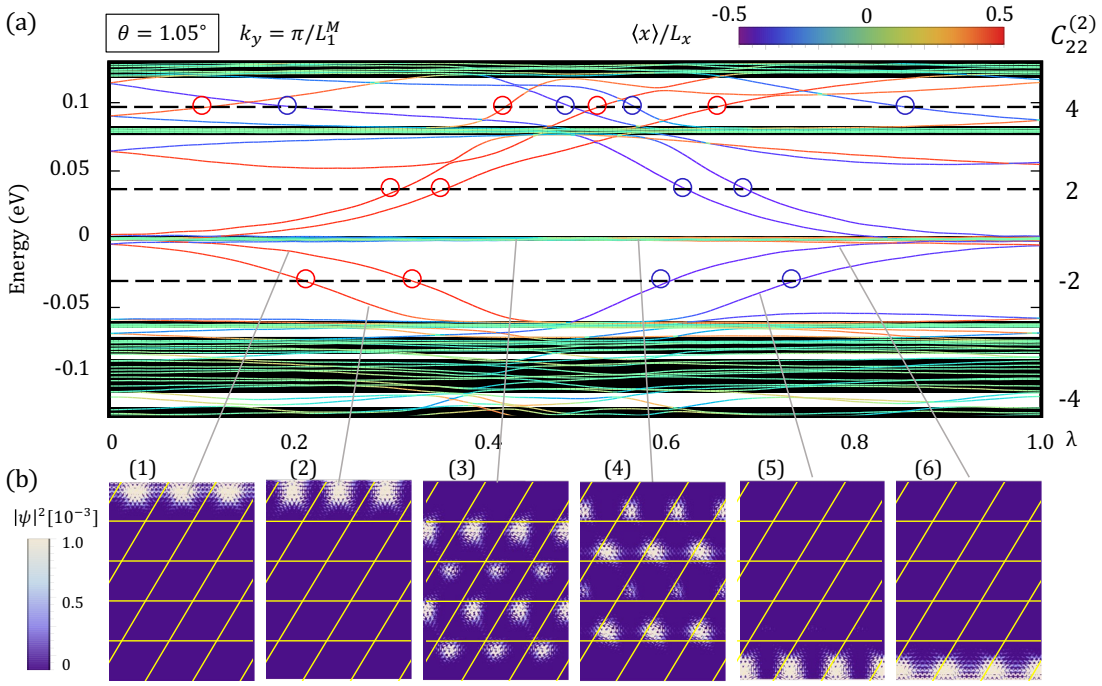

Figure 4.5: (a) The same plot as Fig. 4.4(a). The dashed lines represent the Fermi energies, and the crossing points with edge states are circled. The number of the red or blue circles in the gaps corresponds to the sliding Chern numbers shown on the right side of the figure. (b)Real-space map of low-energy eigenstates of the TBG ribbon.

band, the sliding Chern numbers per spin (summed over valleys) are calculated as $C_{11}^{(1)} = C_{22}^{(1)} = 2$, $C_{11}^{(2)} = C_{22}^{(2)} = -2$ and otherwise 0. [154] If we slide the layer 2 by $\Delta\vec{x}^{(2)} = (1/2)\mathbf{a}_1^{(2)} - \mathbf{a}_2^{(2)}$ as considered for the ribbon, the polarization shift per spin becomes

$$\begin{aligned}\Delta\mathbf{P} &= \frac{1}{2}(C_{11}^{(2)}\mathbf{L}_1^M + C_{12}^{(2)}\mathbf{L}_2^M) - (C_{21}^{(2)}\mathbf{L}_1^M + C_{22}^{(2)}\mathbf{L}_2^M) \\ &= 2\left(-\frac{1}{2}\mathbf{L}_1^M + \mathbf{L}_2^M\right) = 2\Delta\vec{X},\end{aligned} \tag{4.3}$$

where $\Delta\vec{X}$ is the shift of the moiré pattern argued in the previous section. This means that two electrons (per spin) pass through every unit-cell boundary perpendicular to x. Moreover, in the second gap around 0.1 eV, the sliding Chern numbers (per spin) are $C_{11}^{(1)} = C_{22}^{(1)} = 4$, $C_{11}^{(2)} = C_{22}^{(2)} = -4$ and otherwise 0, giving $\Delta\mathbf{P} = 4\Delta\vec{X}$. The number of pumped electrons for each gap is shown on the right side of Fig. 4.5(a).

According to Fig. 2.5, the number of pumped charges through the edge states can be computed from the number of transferred edge states across the gap. The circles in Fig. 4.5(a) represent the intersections of constant energy lines and the edge state bands in each gap. For instance, we consider the Fermi energy lies at 0.04eV. When lambda is changed from 0 to 1, two upper edge-state electrons (red lines) are absorbed to the upper electrode (reservoir), and two lower edge-state electrons (blue lines) are supplied from the lower electrode. In the process, two electrons (per moiré unit cell width) are pumped from the lower side to the upper side, which coincides with the sliding Chern number per spin. The link between the number of transferred edge states across the gap and the sliding Chern number can be found in every gap, and this can be viewed as a bulk edge correspondence in the moiré system.

The edge state pumping and the bulk-edge correspondence in the moiré system are analogous to those in the quantum Hall effect (QHE). [103, 105] In the quantum Hall system, a transfer of the edge states is observed against a change of momentum along the Hall bar. In the moiré pumping, on the other hand, the edge state transfer occurs as a function as a sliding parameter λ, instead of the momentum. This corresponds to the fact that the conventional Chern number for the Hall conductivity σ_{xy} is an integral of the Berry curvature on the (k_x, k_y) space (torus), while the sliding Chern number, Eq. (3.6), is that on the (k_i, λ_j) space.

A notable difference from the QHE is that the sliding Chern number, Eq. (3.6), includes the momentum integration in only a single direction (the charge pumping direction) so that the momentum in the other direction remains as a parameter. In the case of Fig. 4.4, for example, the sliding Chern number is defined for each k_y, and it is topologically protected as long as the energy spectrum at the fixed k_y (and any k_x) is gapped. The bulk-edge correspondence stands at every single k_y, i.e., the sliding Chern number at given k_y corresponds to the number of the pumped edge levels at the k_y, as exactly observed in Fig. 4.4. In the

QHE, in contrast, the Chern number includes the integral in both k_x, k_y, and it is well defined only when the spectrum is gapped on the entire two-dimensional momentum space of (k_x, k_y).

Since the number of transferred edge states during a sliding process is a topological invariant, it is expected to be robust even in the presence of edge disorder. This can be intuitively understood as follows: During the interlayer sliding, the bulk state electrons are pumped towards the edge by the movement of the moiré pattern, and there must be in-gap edge states to absorb the excessive electrons accumulated at the edge regardless of the detailed edge structure.

While the above calculation is limited to the magic angle TBG, the pumping of the edge states occurs in a broad range of twist angle. In Appendix 6.2, we present the plots similar to Fig. 4.4 for $\theta = 1.47°, 2.65°$ and $6.01°$. In increasing the twist angle, we see that the moiré gap between the flat band and the excited band narrows and partially closes in some region of k_y. But we still see the same number of the edge states pumped in the gapped region because the sliding Chern number remains unchanged in the gap. Moreover, the flat bands obtain a dispersion, and edge states emerge around zero energy. The edge state is localized at the zigzag edge and originates from the topology of monolayer graphene. There is no charge pumping from the zero energy edge states because they are not absorbed and released from the flat band. This result corresponds to the zero sliding Chern number for the zero energy gap.

Generally, the sliding Chern number can be non-zero in energy gaps opened by the superlattice interlayer interaction. Any gaps which already exist in the monolayer are trivial in terms of the sliding Chern number because the interlayer interaction can be continuously switched off without closing the gap, and then no moiré pumping takes place.

Chapter 5

Conclusion

In this thesis, we studied the topological phenomena driven by interlayer sliding in the moiré superlattices for 1D and 2D systems.

In Chapter 3, we studied the topological charge pumping driven by interlayer sliding in the moiré superlattices. The number of pumped charges is quantized to the sliding Chern numbers, which can be found as a solution of a Diophantine equation. When the Fermi energy in the energy gap above or below the nearly-flat bands of the TBG, four electrons per superlattice period is conveyed following the flow of the moiré pattern perpendicularly to the sliding direction.

In Chapter 4, we studied the edge states of moiré superlattice systems, such as the double-chain model with terminated one of a pair and the TBG nanoribbon, and the topological correspondence to the moiré sliding. We calculated the eigenspectrum for a single cycle of the sliding process and we demonstrated that the edge states are transferred across the band gap during the interlayer sliding, and the number of edge states pumped in the sliding cycle coincides with the sliding Chern number of the band gap. The relationship can be viewed as a manifestation of the bulk-edge correspondence in moiré systems, where a nonzero sliding Chern number is always associated with the emergence of moiré edge states.

From a future perspective, the charge pumping proposed in this thesis has a potential application to a new class of power source devices. The charge pumping by moire sliding converts the mechanical motion of the atomic layer to electric current. We expect that it can be a good platform of nanogenerators by using van der Waals layered materials in the future. In addition, the opposite effect, which converts the in-plane DC voltage to mechanical motion, can also be expected. It

may be useful to realize the atomic scale nanomotors.

The moiré charge pumping by interlayer sliding is expected also in other superlattices whenever the Fermi energy is in an energy gap with non-zero sliding Chern number. For example, moiré bilayer such as the graphene/hBN system [69, 70, 157, 158, 72, 74, 73, 75, 76] and twisted bilayers of transition metal dichalcogenides[23, 159, 25, 26, 160, 161] have been synthesized. Moreover, the theory could be directly applicable to quasiparticles other than electrons such as phonon[79, 80, 84], exciton[162, 25, 160, 161], Majorana fermion[163, 164, 165], magnon[32, 33, 34, 35, 36, 37, 38], and skyrmion[166, 33, 167, 37, 38].

Chapter 6

Appendix

6.1 Sliding Chern number of a single valley

Here we prove the sliding Chern numbers of K and K' are equal due to the time reversal symmetry. The (spinless) continuum Hamiltonian for the low-angle TBG is written as

$$\mathcal{H}_\xi(\mathbf{k},\boldsymbol{\lambda}) = \begin{pmatrix} H^1_\xi(\mathbf{k}) & U^\dagger_\xi(\mathbf{k},\boldsymbol{\lambda}) \\ U_\xi(\mathbf{k},\boldsymbol{\lambda}) & H^2_\xi(\mathbf{k}) \end{pmatrix} \tag{6.1}$$

where $\xi = K, K'$ is the valley index, $\boldsymbol{\lambda}$ is the sliding vector, H^l $(l = 1, 2)$ is the Hamiltonian for monolayer graphene and U is the interlayer coupling. The Hamiltonians for the opposite valleys are related by time reversal operation,

$$\mathcal{T}\mathcal{H}_K(\mathbf{k},\boldsymbol{\lambda})\mathcal{T}^\dagger = \mathcal{H}_{K'}(-\mathbf{k},\boldsymbol{\lambda}), \tag{6.2}$$

where $\mathcal{T} = \mathcal{K}$ is the complex conjugation operator. Therefore its eigenvalues and Bloch wave functions follow

$$\begin{aligned} E_{K,n}(\mathbf{k},\boldsymbol{\lambda}) &= E_{K',n}(-\mathbf{k},\boldsymbol{\lambda}), \\ u_{K,n}(\mathbf{k},\boldsymbol{\lambda}) &= u^*_{K',n}(-\mathbf{k},\boldsymbol{\lambda}). \end{aligned} \tag{6.3}$$

We define the sliding Chern numbers of a single valley as

$$C^{(l)}_{ij}(\xi) = \sum_{n=\text{ occupied}} \int_0^1 dk_j \int_0^1 d\lambda_i \Omega^\xi(k_j, \lambda_i) \tag{6.4}$$

where

$$\Omega^{\xi}(k_j, \lambda_i) = i \left[\left\langle \frac{\partial u_\xi}{\partial \lambda_i} \middle| \frac{\partial u_\xi}{\partial k_j} \right\rangle - \left\langle \frac{\partial u_\xi}{\partial k_j} \middle| \frac{\partial u_\xi}{\partial \lambda_i} \right\rangle \right] \tag{6.5}$$

is the Berry curvature in (k_j, λ_i) parameter space. From Eq. (6.3) and Eq. (6.5), the Berry curvatures of the opposite valleys are related by

$$\Omega^{K}(k_j, \lambda_i) = \Omega^{K'}(-k_j, \lambda_i), \tag{6.6}$$

which finally leads to

$$C_{ij}^{(l)}(K) = C_{ij}^{(l)}(K'). \tag{6.7}$$

6.2 Moiré edge states in other twist angles

In the main text, we calculated the energy spectrum of the TBG ribbon with $\theta = 1.05^\circ$ [Fig. 4.4], where we showed the emergence of the edge states is related by non-zero sliding Chern number. Actually, the edge states exist in other twisted angles, as long as the gap remains opens at each k_y. Here we present the plots similar to Fig. 4.4 calculated for TBG ribbons of $\theta = 1.47^\circ, 2.65^\circ$ and 6.01° in Figs. 6.1, 6.2 and 6.3, respectively. In increasing the twist angle from 1.05°, the moiré gap between the flat band and the excited band partially closes in some region of k_y. But still, we see the same number of the edge-state pumping in the gapped region, because the sliding Chern number remains unchanged in the gap.

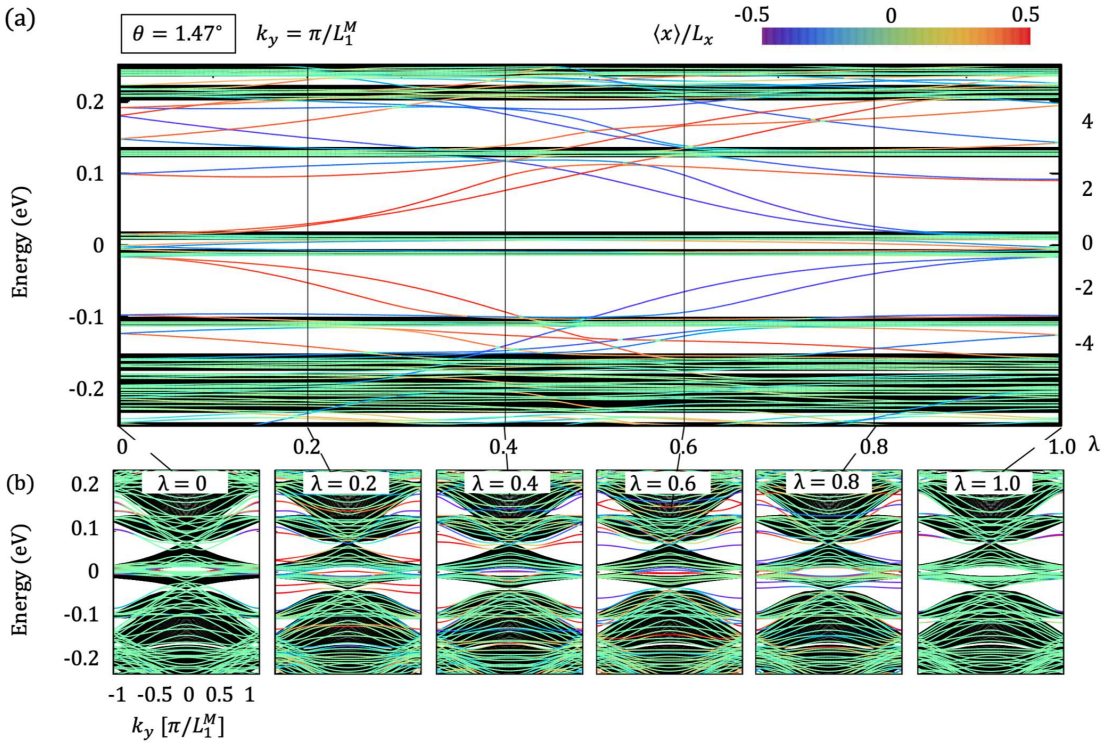

Figure 6.1: Plot similar to Fig. 4.4 calculated for TBG ribbons of $\theta = 1.47°$.

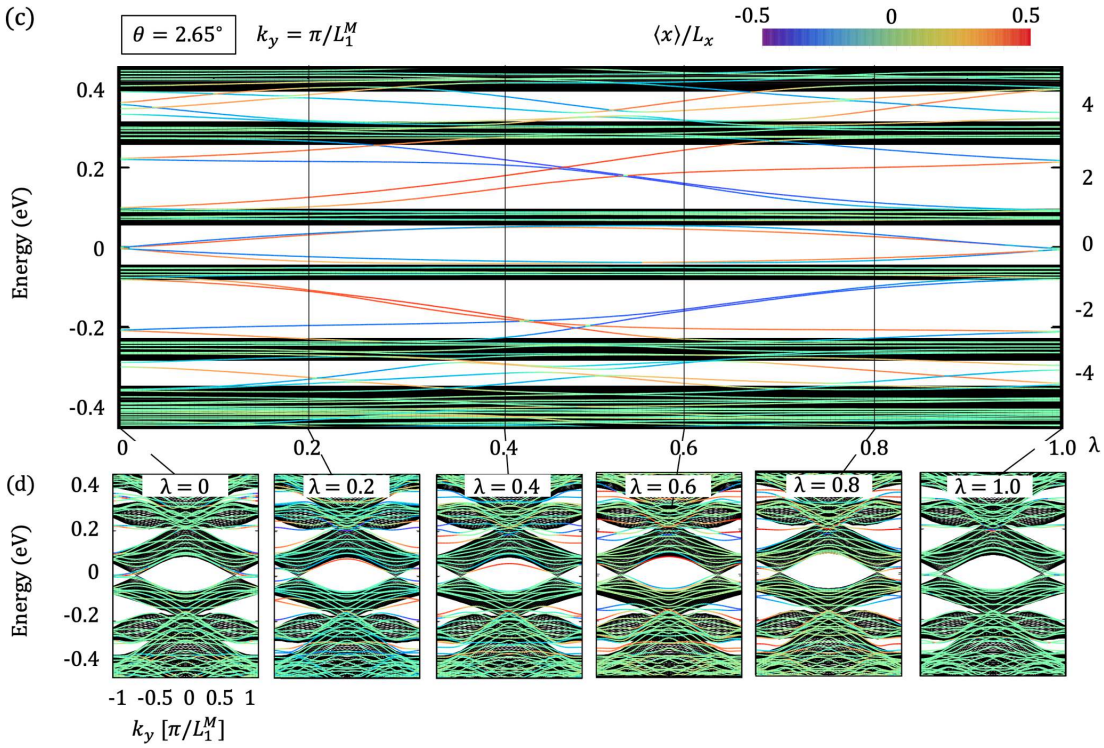

Figure 6.2: Plot similar to Fig. 4.4 calculated for TBG ribbons of $\theta = 2.65°$.

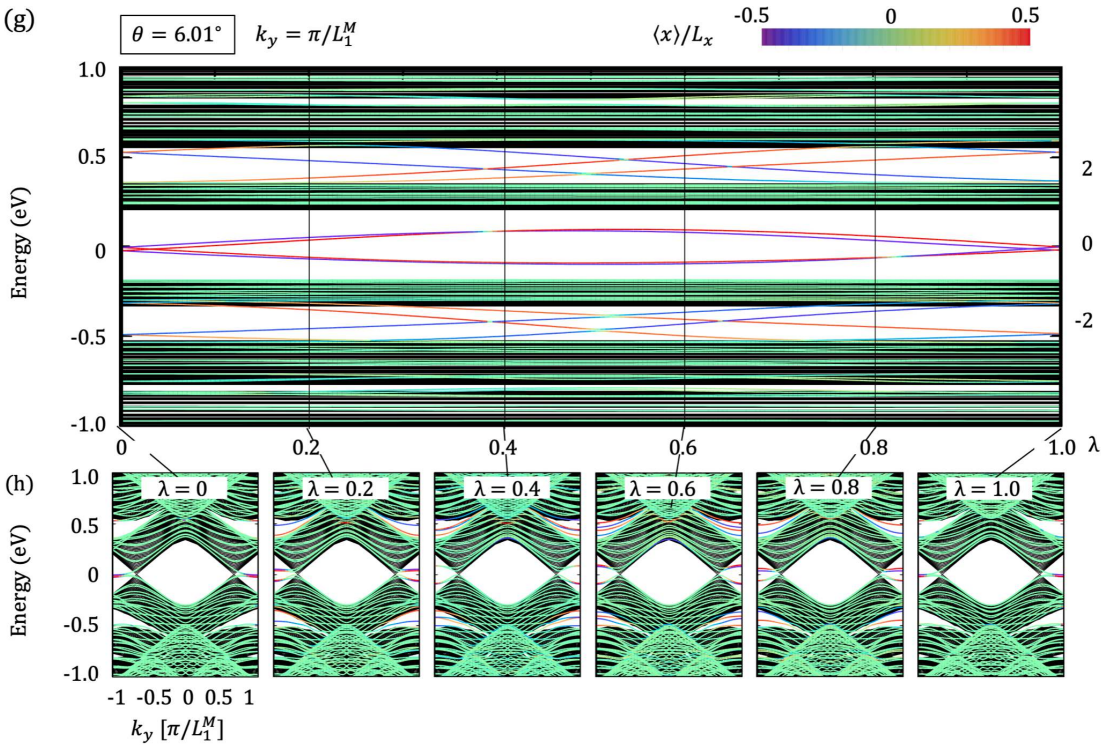

Figure 6.3: Plot similar to Fig. 4.4 calculated for TBG ribbons of $\theta = 6.01°$.

Bibliography

[1] J. M. B. Lopes dos Santos, N. M. R. Peres, and A. H. Castro Neto, "Graphene bilayer with a twist: Electronic structure," *Physical Review Letters*, vol. 99, p. 256802, Dec 2007.

[2] E. J. Mele, "Commensuration and interlayer coherence in twisted bilayer graphene," *Physical Review B*, vol. 81, p. 161405, Apr 2010.

[3] G. Trambly de Laissardière, D. Mayou, and L. Magaud, "Localization of dirac electrons in rotated graphene bilayers," *Nano letters*, vol. 10, no. 3, pp. 804–808, 2010.

[4] S. Shallcross, S. Sharma, E. Kandelaki, and O. Pankratov, "Electronic structure of turbostratic graphene," *Physical Review B*, vol. 81, no. 16, p. 165105, 2010.

[5] E. Suárez Morell, J. D. Correa, P. Vargas, M. Pacheco, and Z. Barticevic, "Flat bands in slightly twisted bilayer graphene: Tight-binding calculations," *Physical Review B*, vol. 82, p. 121407, Sep 2010.

[6] R. Bistritzer and A. H. MacDonald, "Moiré bands in twisted double-layer graphene," *Proceedings of the National Academy of Sciences*, vol. 108, no. 30, pp. 12 233–12 237, 2011.

[7] M. Kindermann and P. N. First, "Local sublattice-symmetry breaking in rotationally faulted multilayer graphene," *Physical Review B*, vol. 83, p. 045425, Jan 2011.

[8] L. Xian, S. Barraza-Lopez, and M. Y. Chou, "Effects of electrostatic fields and charge doping on the linear bands in twisted graphene bilayers," *Physical Review B*, vol. 84, p. 075425, Aug 2011.

[9] J. M. B. Lopes dos Santos, N. M. R. Peres, and A. H. Castro Neto, "Continuum model of the twisted graphene bilayer," *Physical Review B*, vol. 86, p. 155449, Oct 2012.

[10] P. Moon and M. Koshino, "Energy spectrum and quantum hall effect in twisted bilayer graphene," *Physical Review B*, vol. 85, p. 195458, May 2012.

[11] G. Trambly de Laissardière, D. Mayou, and L. Magaud, "Numerical studies of confined states in rotated bilayers of graphene," *Physical Review B*, vol. 86, p. 125413, Sep 2012.

[12] P. Moon and M. Koshino, "Optical absorption in twisted bilayer graphene," *Physical Review B*, vol. 87, p. 205404, May 2013.

[13] Y. Cao, V. Fatemi, S. Fang, K. Watanabe, T. Taniguchi, E. Kaxiras, and P. Jarillo-Herrero, "Unconventional superconductivity in magic-angle graphene superlattices," *Nature*, vol. 556, no. 7699, pp. 43–50, 2018.

[14] M. Yankowitz, S. Chen, H. Polshyn, Y. Zhang, K. Watanabe, T. Taniguchi, D. Graf, A. F. Young, and C. R. Dean, "Tuning superconductivity in twisted bilayer graphene," *Science*, vol. 363, no. 6431, pp. 1059–1064, 2019.

[15] X. Lu, P. Stepanov, W. Yang, M. Xie, M. A. Aamir, I. Das, C. Urgell, K. Watanabe, T. Taniguchi, G. Zhang *et al.*, "Superconductors, orbital magnets and correlated states in magic-angle bilayer graphene," *Nature*, vol. 574, no. 7780, pp. 653–657, 2019.

[16] Y. Cao, V. Fatemi, A. Demir, S. Fang, S. L. Tomarken, J. Y. Luo, J. D. Sanchez-Yamagishi, K. Watanabe, T. Taniguchi, E. Kaxiras *et al.*, "Correlated insulator behaviour at half-filling in magic-angle graphene superlattices," *Nature*, vol. 556, no. 7699, pp. 80–84, 2018.

[17] J. Y. Lee, E. Khalaf, S. Liu, X. Liu, Z. Hao, P. Kim, and A. Vishwanath, "Theory of correlated insulating behaviour and spin-triplet superconductivity in twisted double bilayer graphene," *Nat. Commun.*, vol. 10, no. 1, pp. 1–10, 2019.

[18] X. Liu, Z. Hao, E. Khalaf, J. Y. Lee, Y. Ronen, H. Yoo, D. Haei Najafabadi, K. Watanabe, T. Taniguchi, A. Vishwanath *et al.*, "Tunable spin-polarized correlated states in twisted double bilayer graphene," *Nature*, vol. 583, no. 7815, pp. 221–225, 2020.

[19] C. Shen, Y. Chu, Q. Wu, N. Li, S. Wang, Y. Zhao, J. Tang, J. Liu, J. Tian, K. Watanabe *et al.*, "Correlated states in twisted double bilayer graphene," *Nature Physics*, vol. 16, no. 5, pp. 520–525, 2020.

[20] M. He, Y. Li, J. Cai, Y. Liu, K. Watanabe, T. Taniguchi, X. Xu, and M. Yankowitz, "Symmetry breaking in twisted double bilayer graphene," *Nature Physics*, vol. 17, no. 1, pp. 26–30, 2021.

[21] J. M. Park, Y. Cao, K. Watanabe, T. Taniguchi, and P. Jarillo-Herrero, "Tunable strongly coupled superconductivity in magic-angle twisted trilayer graphene," *Nature*, vol. 590, no. 7845, pp. 249–255, 2021.

[22] P. Rivera, J. R. Schaibley, A. M. Jones, J. S. Ross, S. Wu, G. Aivazian, P. Klement, K. Seyler, G. Clark, N. J. Ghimire *et al.*, "Observation of long-lived interlayer excitons in monolayer mose2–wse2 heterostructures," *Nature communications*, vol. 6, no. 1, pp. 1–6, 2015.

[23] F. Wu, T. Lovorn, E. Tutuc, and A. H. MacDonald, "Hubbard model physics in transition metal dichalcogenide moiré bands," *Physical Review Letters*, vol. 121, p. 026402, Jul 2018.

[24] F. Wu, T. Lovorn, E. Tutuc, I. Martin, and A. MacDonald, "Topological insulators in twisted transition metal dichalcogenide homobilayers," *Physical Review Letters*, vol. 122, no. 8, p. 086402, 2019.

[25] K. L. Seyler, P. Rivera, H. Yu, N. P. Wilson, E. L. Ray, D. G. Mandrus, J. Yan, W. Yao, and X. Xu, "Signatures of moiré-trapped valley excitons in mose2/wse2 heterobilayers," *Nature*, vol. 567, no. 7746, pp. 66–70, 2019.

[26] K. Tran, G. Moody, F. Wu, X. Lu, J. Choi, K. Kim, A. Rai, D. A. Sanchez, J. Quan, A. Singh *et al.*, "Evidence for moiré excitons in van der waals heterostructures," *Nature*, vol. 567, no. 7746, pp. 71–75, 2019.

[27] T. Wang, S. Miao, Z. Li, Y. Meng, Z. Lu, Z. Lian, M. Blei, T. Taniguchi, K. Watanabe, S. Tongay *et al.*, "Giant valley-zeeman splitting from spin-singlet and spin-triplet interlayer excitons in wse2/mose2 heterostructure," *Nano letters*, vol. 20, no. 1, pp. 694–700, 2019.

[28] L. Wang, E.-M. Shih, A. Ghiotto, L. Xian, D. A. Rhodes, C. Tan, M. Claassen, D. M. Kennes, Y. Bai, B. Kim *et al.*, "Correlated electronic phases in twisted bilayer transition metal dichalcogenides," *Nature materials*, vol. 19, no. 8, pp. 861–866, 2020.

[29] Y. Shimazaki, I. Schwartz, K. Watanabe, T. Taniguchi, M. Kroner, and A. Imamoğlu, "Strongly correlated electrons and hybrid excitons in a moiré heterostructure," *Nature*, vol. 580, no. 7804, pp. 472–477, 2020.

[30] A. Ghiotto, E.-M. Shih, G. S. Pereira, D. A. Rhodes, B. Kim, J. Zang, A. J. Millis, K. Watanabe, T. Taniguchi, J. C. Hone *et al.*, "Quantum criticality in twisted transition metal dichalcogenides," *Nature*, vol. 597, no. 7876, pp. 345–349, 2021.

[31] S. Miao, T. Wang, X. Huang, D. Chen, Z. Lian, C. Wang, M. Blei, T. Taniguchi, K. Watanabe, S. Tongay *et al.*, "Strong interaction between interlayer excitons and correlated electrons in wse2/ws2 moiré superlattice," *Nature communications*, vol. 12, no. 1, pp. 1–6, 2021.

[32] Q. Tong, F. Liu, J. Xiao, and W. Yao, "Skyrmions in the moiré of van der waals 2d magnets," *Nano letters*, vol. 18, no. 11, pp. 7194–7199, 2018.

[33] C. Wang, Y. Gao, H. Lv, X. Xu, and D. Xiao, "Stacking domain wall magnons in twisted van der waals magnets," *Physical Review Letters*, vol. 125, no. 24, p. 247201, 2020.

[34] K. Hejazi, Z.-X. Luo, and L. Balents, "Noncollinear phases in moiré magnets," *Proceedings of the National Academy of Sciences*, vol. 117, no. 20, pp. 10 721–10 726, 2020.

[35] K. Hejazi, Z.-X. Luo, L. Balents *et al.*, "Heterobilayer moiré magnets: Moiré skyrmions and commensurate-incommensurate transitions," *Physical Review B*, vol. 104, no. 10, p. L100406, 2021.

[36] M. Akram and O. Erten, "Skyrmions in twisted van der waals magnets," *Physical Review B*, vol. 103, no. 14, p. L140406, 2021.

[37] F. Xiao, K. Chen, and Q. Tong, "Magnetization textures in twisted bilayer cr x 3 (x= br, i)," *Physical Review Research*, vol. 3, no. 1, p. 013027, 2021.

[38] H. Xie, X. Luo, G. Ye, Z. Ye, H. Ge, S. H. Sung, E. Rennich, S. Yan, Y. Fu, S. Tian *et al.*, "Twist engineering of the two-dimensional magnetism in double bilayer chromium triiodide homostructures," *Nature Physics*, vol. 18, no. 1, pp. 30–36, 2022.

[39] D. M. Kennes, L. Xian, M. Claassen, and A. Rubio, "One-dimensional flat bands in twisted bilayer germanium selenide," *Nat. Commun.*, vol. 11, no. 1, pp. 1–8, 2020.

[40] M. Fujimoto and T. Kariyado, "Effective continuum model of twisted bilayer gese and origin of the emerging one-dimensional mode," *Physical Review B*, vol. 104, no. 12, p. 125427, 2021.

[41] J. An and J. Kang, "Emergence and tuning of multiple flat bands in twisted bilayer γ-graphyne," *Journal of Physical Chemistry Letter*, vol. 12, pp. 12 283–12 291, 2021.

[42] K. Yasuda, X. Wang, K. Watanabe, T. Taniguchi, and P. Jarillo-Herrero, "Stacking-engineered ferroelectricity in bilayer boron nitride," *Science*, vol. 372, no. 6549, pp. 1458–1462, 2021.

[43] C. Woods, P. Ares, H. Nevison-Andrews, M. Holwill, R. Fabregas, F. Guinea, A. Geim, K. Novoselov, N. Walet, and L. Fumagalli, "Charge-polarized interfacial superlattices in marginally twisted hexagonal boron nitride," *Nature communications*, vol. 12, no. 1, pp. 1–7, 2021.

[44] S. Moore, C. Ciccarino, D. Halbertal, L. McGilly, N. Finney, K. Yao, Y. Shao, G. Ni, A. Sternbach, E. Telford *et al.*, "Nanoscale lattice dynamics in hexagonal boron nitride moiré superlattices," *Nature communications*, vol. 12, no. 1, pp. 1–7, 2021.

[45] K. S. Novoselov, A. K. Geim, S. V. Morozov, D.-e. Jiang, Y. Zhang, S. V. Dubonos, I. V. Grigorieva, and A. A. Firsov, "Electric field effect in atomically thin carbon films," *science*, vol. 306, no. 5696, pp. 666–669, 2004.

[46] M. Koshino, N. F. Q. Yuan, T. Koretsune, M. Ochi, K. Kuroki, and L. Fu, "Maximally localized wannier orbitals and the extended hubbard model for twisted bilayer graphene," *Physical Review X*, vol. 8, p. 031087, Sep 2018.

[47] H. C. Po, L. Zou, T. Senthil, and A. Vishwanath, "Faithful tight-binding models and fragile topology of magic-angle bilayer graphene," *Physical Review B*, vol. 99, no. 19, p. 195455, 2019.

[48] J. Ahn, S. Park, and B.-J. Yang, "Failure of nielsen-ninomiya theorem and fragile topology in two-dimensional systems with space-time inversion symmetry: application to twisted bilayer graphene at magic angle," *Physical Review X*, vol. 9, no. 2, p. 021013, 2019.

[49] Z. Song, Z. Wang, W. Shi, G. Li, C. Fang, and B. A. Bernevig, "All magic angles in twisted bilayer graphene are topological," *Physical Review Letters*, vol. 123, no. 3, p. 036401, 2019.

[50] S. Carr, S. Fang, H. C. Po, A. Vishwanath, and E. Kaxiras, "Derivation of wannier orbitals and minimal-basis tight-binding hamiltonians for twisted bilayer graphene: First-principles approach," *Physical Review Research*, vol. 1, no. 3, p. 033072, 2019.

[51] Z.-D. Song, L. Elcoro, and B. A. Bernevig, "Twisted bulk-boundary correspondence of fragile topology," *Science*, vol. 367, no. 6479, pp. 794–797, 2020.

[52] F. Wu, A. H. MacDonald, and I. Martin, "Theory of phonon-mediated superconductivity in twisted bilayer graphene," *Physical Review Letters*, vol. 121, no. 25, p. 257001, 2018.

[53] C. Xu and L. Balents, "Topological superconductivity in twisted multilayer graphene," *Physical Review Letters*, vol. 121, no. 8, p. 087001, 2018.

[54] H. Isobe, N. F. Yuan, and L. Fu, "Unconventional superconductivity and density waves in twisted bilayer graphene," *Physical Review X*, vol. 8, no. 4, p. 041041, 2018.

[55] Y.-Z. You and A. Vishwanath, "Superconductivity from valley fluctuations and approximate so (4) symmetry in a weak coupling theory of twisted bilayer graphene," *npj Quantum Materials*, vol. 4, no. 1, pp. 1–12, 2019.

[56] B. Lian, Z. Wang, and B. A. Bernevig, "Twisted bilayer graphene: a phonon-driven superconductor," *Physical Review Letters*, vol. 122, no. 25, p. 257002, 2019.

[57] L. Classen, A. V. Chubukov, C. Honerkamp, and M. M. Scherer, "Competing orders at higher-order van hove points," *Physical Review B*, vol. 102, no. 12, p. 125141, 2020.

[58] D. V. Chichinadze, L. Classen, and A. V. Chubukov, "Valley magnetism, nematicity, and density wave orders in twisted bilayer graphene," *Physical Review B*, vol. 102, no. 12, p. 125120, 2020.

[59] R. M. Fernandes and J. W. Venderbos, "Nematicity with a twist: Rotational symmetry breaking in a moiré superlattice," *Science Advances*, vol. 6, no. 32, p. eaba8834, 2020.

[60] Y. Saito, J. Ge, K. Watanabe, T. Taniguchi, and A. F. Young, "Independent superconductors and correlated insulators in twisted bilayer graphene," *Nature Physics*, vol. 16, no. 9, pp. 926–930, 2020.

[61] Y. Wang, J. Kang, and R. M. Fernandes, "Topological and nematic superconductivity mediated by ferro-su (4) fluctuations in twisted bilayer graphene," *Physical Review B*, vol. 103, no. 2, p. 024506, 2021.

[62] S. Chatterjee, M. Ippoliti, and M. P. Zaletel, "Skyrmion superconductivity: Dmrg evidence for a topological route to superconductivity," *Physical Review B*, vol. 106, no. 3, p. 035421, 2022.

[63] G. Tarnopolsky, A. J. Kruchkov, and A. Vishwanath, "Origin of magic angles in twisted bilayer graphene," *Physical Review Letters*, vol. 122, no. 10, p. 106405, 2019.

[64] K. F. Mak and J. Shan, "Semiconductor moiré materials," *Nature Nanotechnology*, vol. 17, no. 7, pp. 686–695, 2022.

[65] R. Decker, Y. Wang, V. W. Brar, W. Regan, H.-Z. Tsai, Q. Wu, W. Gannett, A. Zettl, and M. F. Crommie, "Local electronic properties of graphene on a bn substrate via scanning tunneling microscopy," *Nano letters*, vol. 11, no. 6, pp. 2291–2295, 2011.

[66] J. Xue, J. Sanchez-Yamagishi, D. Bulmash, P. Jacquod, A. Deshpande, K. Watanabe, T. Taniguchi, P. Jarillo-Herrero, and B. J. LeRoy, "Scanning tunnelling microscopy and spectroscopy of ultra-flat graphene on hexagonal boron nitride," *Nature materials*, vol. 10, no. 4, pp. 282–285, 2011.

[67] M. Yankowitz, J. Xue, D. Cormode, J. D. Sanchez-Yamagishi, K. Watanabe, T. Taniguchi, P. Jarillo-Herrero, P. Jacquod, and B. J. LeRoy, "Emergence of superlattice dirac points in graphene on hexagonal boron nitride," *Nature physics*, vol. 8, no. 5, pp. 382–386, 2012.

[68] M. Yankowitz, Q. Ma, P. Jarillo-Herrero, and B. J. LeRoy, "van der waals heterostructures combining graphene and hexagonal boron nitride," *Nature Reviews Physics*, vol. 1, no. 2, pp. 112–125, 2019.

[69] M. Kindermann, B. Uchoa, and D. L. Miller, "Zero-energy modes and gate-tunable gap in graphene on hexagonal boron nitride," *Physical Review B*, vol. 86, p. 115415, Sep 2012.

[70] J. R. Wallbank, A. A. Patel, M. Mucha-Kruczyński, A. K. Geim, and V. I. Fal'ko, "Generic miniband structure of graphene on a hexagonal substrate," *Physical Review B*, vol. 87, p. 245408, Jun 2013.

[71] J. C. Song, A. V. Shytov, and L. S. Levitov, "Electron interactions and gap opening in graphene superlattices," *Physical Review Letters*, vol. 111, no. 26, p. 266801, 2013.

[72] P. Moon and M. Koshino, "Electronic properties of graphene/hexagonal-boron-nitride moiré superlattice," *Physical Review B*, vol. 90, no. 15, p. 155406, 2014.

[73] L. Ponomarenko, R. Gorbachev, G. Yu, D. Elias, R. Jalil, A. Patel, A. Mishchenko, A. Mayorov, C. Woods, J. Wallbank *et al.*, "Cloning of dirac fermions in graphene superlattices," *Nature*, vol. 497, no. 7451, pp. 594–597, 2013.

[74] C. R. Dean, L. Wang, P. Maher, C. Forsythe, F. Ghahari, Y. Gao, J. Katoch, M. Ishigami, P. Moon, M. Koshino *et al.*, "Hofstadter's butterfly and the fractal quantum hall effect in moiré superlattices," *Nature*, vol. 497, no. 7451, pp. 598–602, 2013.

[75] B. Hunt, J. D. Sanchez-Yamagishi, A. F. Young, M. Yankowitz, B. J. LeRoy, K. Watanabe, T. Taniguchi, P. Moon, M. Koshino, P. Jarillo-Herrero *et al.*, "Massive dirac fermions and hofstadter butterfly in a van der waals heterostructure," *Science*, vol. 340, no. 6139, pp. 1427–1430, 2013.

[76] G. Yu, R. Gorbachev, J. Tu, A. Kretinin, Y. Cao, R. Jalil, F. Withers, L. Ponomarenko, B. Piot, M. Potemski *et al.*, "Hierarchy of hofstadter states and replica quantum hall ferromagnetism in graphene superlattices," *Nature physics*, vol. 10, no. 7, pp. 525–529, 2014.

[77] L. Wang, Y. Gao, B. Wen, Z. Han, T. Taniguchi, K. Watanabe, M. Koshino, J. Hone, and C. R. Dean, "Evidence for a fractional fractal quantum hall effect in graphene superlattices," *Science*, vol. 350, no. 6265, pp. 1231–1234, 2015.

[78] R. Krishna Kumar, X. Chen, G. Auton, A. Mishchenko, D. A. Bandurin, S. V. Morozov, Y. Cao, E. Khestanova, M. Ben Shalom, A. Kretinin *et al.*, "High-temperature quantum oscillations caused by recurring bloch states in graphene superlattices," *Science*, vol. 357, no. 6347, pp. 181–184, 2017.

[79] M. Koshino and Y.-W. Son, "Moiré phonons in twisted bilayer graphene," *Physical Review B*, vol. 100, no. 7, p. 075416, 2019.

[80] H. Ochoa, "Moiré-pattern fluctuations and electron-phason coupling in twisted bilayer graphene," *Physical Review B*, vol. 100, no. 15, p. 155426, 2019.

[81] I. Maity, M. H. Naik, P. K. Maiti, H. Krishnamurthy, and M. Jain, "Phonons in twisted transition-metal dichalcogenide bilayers: ultrasoft phasons and a transition from a superlubric to a pinned phase," *Physical Review Research*, vol. 2, no. 1, p. 013335, 2020.

[82] A. C. Gadelha, D. A. Ohlberg, C. Rabelo, E. G. Neto, T. L. Vasconcelos, J. L. Campos, J. S. Lemos, V. Ornelas, D. Miranda, R. Nadas *et al.*, "Localization of lattice dynamics in low-angle twisted bilayer graphene," *Nature*, vol. 590, no. 7846, pp. 405–409, 2021.

[83] J. Quan, L. Linhart, M.-L. Lin, D. Lee, J. Zhu, C.-Y. Wang, W.-T. Hsu, J. Choi, J. Embley, C. Young *et al.*, "Phonon renormalization in reconstructed mos2 moiré superlattices," *Nature materials*, vol. 20, no. 8, pp. 1100–1105, 2021.

[84] N. Suri, C. Wang, Y. Zhang, and D. Xiao, "Chiral phonons in moiré superlattices," *Nano letters*, vol. 21, no. 23, pp. 10 026–10 031, 2021.

[85] F. Wu, E. Hwang, and S. D. Sarma, "Phonon-induced giant linear-in-t resistivity in magic angle twisted bilayer graphene: Ordinary strangeness and exotic superconductivity," *Physical Review B*, vol. 99, no. 16, p. 165112, 2019.

[86] H. Ishizuka, A. Fahimniya, F. Guinea, and L. Levitov, "Purcell-like enhancement of electron–phonon interactions in long-period superlattices: Linear-temperature resistivity and cooling power," *Nano Letters*, vol. 21, no. 18, pp. 7465–7471, 2021.

[87] S. Han, X. Nie, S. Gu, W. Liu, L. Chen, H. Ying, L. Wang, Z. Cheng, L. Zhao, and S. Chen, "Twist-angle-dependent thermal conduction in single-crystalline bilayer graphene," *Applied Physics Letters*, vol. 118, no. 19, p. 193104, 2021.

[88] X. Qian, J. Zhou, and G. Chen, "Phonon-engineered extreme thermal conductivity materials," *Nature Materials*, vol. 20, no. 9, pp. 1188–1202, 2021.

[89] D. J. Thouless, "Quantization of particle transport," *Physical Review B*, vol. 27, pp. 6083–6087, May 1983.

[90] S. Nakajima, T. Tomita, S. Taie, T. Ichinose, H. Ozawa, L. Wang, M. Troyer, and Y. Takahashi, "Topological thouless pumping of ultracold fermions," *Nature Physics*, vol. 12, no. 4, pp. 296–300, 2016.

[91] M. Lohse, C. Schweizer, O. Zilberberg, M. Aidelsburger, and I. Bloch, "A thouless quantum pump with ultracold bosonic atoms in an optical superlattice," *Nature Physics*, vol. 12, no. 4, pp. 350–354, 2016.

[92] H.-I. Lu, M. Schemmer, L. M. Aycock, D. Genkina, S. Sugawa, and I. B. Spielman, "Geometrical pumping with a bose-einstein condensate," *Physical Review Letters*, vol. 116, no. 20, p. 200402, 2016.

[93] J.-T. A. Chiang and Q. Niu, "Quantum adiabatic particle transport in optical lattices," *Physical Review A*, vol. 57, pp. R2278–R2280, Apr 1998.

[94] Y. Qian, M. Gong, and C. Zhang, "Quantum transport of bosonic cold atoms in double-well optical lattices," *Physical Review A*, vol. 84, p. 013608, Jul 2011.

[95] L. Wang, M. Troyer, and X. Dai, "Topological charge pumping in a one-dimensional optical lattice," *Physical Review Letters*, vol. 111, p. 026802, Jul 2013.

[96] F. Matsuda, M. Tezuka, and N. Kawakami, "Topological properties of ultracold bosons in one-dimensional quasiperiodic optical lattice," *Journal of the Physical Society of Japan*, vol. 83, no. 8, p. 083707, 2014.

[97] F. Mei, J.-B. You, D.-W. Zhang, X. C. Yang, R. Fazio, S.-L. Zhu, and L. C. Kwek, "Topological insulator and particle pumping in a one-dimensional shaken optical lattice," *Physical Review A*, vol. 90, p. 063638, Dec 2014.

[98] R. Wei and E. J. Mueller, "Anomalous charge pumping in a one-dimensional optical superlattice," *Physical Review A*, vol. 92, p. 013609, Jul 2015.

[99] Y.-B. Yang, L.-M. Duan, and Y. Xu, "Continuously tunable topological pump in high-dimensional cold atomic gases," *Physical Review B*, vol. 98, p. 165128, Oct 2018.

[100] D. J. Thouless, M. Kohmoto, M. P. Nightingale, and M. den Nijs, "Quantized hall conductance in a two-dimensional periodic potential," *Physical Review Letters*, vol. 49, pp. 405–408, Aug 1982.

[101] R. B. Laughlin, "Quantized hall conductivity in two dimensions," *Physical Review B*, vol. 23, pp. 5632–5633, May 1981.

[102] ——, "Nobel lecture: Fractional quantization," *Review Modern Physics*, vol. 71, pp. 863–874, Jul 1999.

[103] Y. Hatsugai, "Chern number and edge states in the integer quantum hall effect," *Physical Review Letters*, vol. 71, pp. 3697–3700, Nov 1993.

[104] B. I. Halperin, "Quantized hall conductance, current-carrying edge states, and the existence of extended states in a two-dimensional disordered potential," *Physical Review B*, vol. 25, pp. 2185–2190, Feb 1982.

[105] Y. Hatsugai, "Edge states in the integer quantum hall effect and the riemann surface of the bloch function," *Physical Review B*, vol. 48, pp. 11 851–11 862, Oct 1993.

[106] A. Y. Kitaev, "Unpaired majorana fermions in quantum wires," *Physics-Uspekhi*, vol. 44, no. 10S, p. 131, oct 2001.

[107] C. L. Kane and E. J. Mele, "Z_2 topological order and the quantum spin hall effect," *Physical Review Letters*, vol. 95, p. 146802, Sep 2005.

[108] B. A. Bernevig, T. L. Hughes, and S.-C. Zhang, "Quantum spin hall effect and topological phase transition in hgte quantum wells," *science*, vol. 314, no. 5806, pp. 1757–1761, 2006.

[109] G. M. Graf and M. Porta, "Bulk-edge correspondence for two-dimensional topological insulators," *Communications in Mathematical Physics*, vol. 324, no. 3, pp. 851–895, 2013.

[110] F. Schindler, A. M. Cook, M. G. Vergniory, Z. Wang, S. S. Parkin, B. A. Bernevig, and T. Neupert, "Higher-order topological insulators," *Science advances*, vol. 4, no. 6, p. eaat0346, 2018.

[111] Y. E. Kraus, Y. Lahini, Z. Ringel, M. Verbin, and O. Zilberberg, "Topological states and adiabatic pumping in quasicrystals," *Physical Review Letters*, vol. 109, p. 106402, Sep 2012.

[112] Y. Hatsugai and T. Fukui, "Bulk-edge correspondence in topological pumping," *Physical Review B*, vol. 94, no. 4, p. 041102, 2016.

[113] W. Landgraf, S. Shallcross, K. Türschmann, D. Weckbecker, and O. Pankratov, "Electronic structure of twisted graphene flakes," *Physical Review B*, vol. 87, p. 075433, Feb 2013.

[114] E. Suárez Morell, R. Vergara, M. Pacheco, L. Brey, and L. Chico, "Electronic properties of twisted bilayer nanoribbons," *Physical Review B*, vol. 89, p. 205405, May 2014.

[115] E. S. Morell, P. Vargas, P. Häberle, S. A. Hevia, and L. Chico, "Edge states of moiré structures in graphite," *Physical Review B*, vol. 91, p. 035441, Jan 2015.

[116] M. Pelc, E. S. Morell, L. Brey, and L. Chico, "Electronic conductance of twisted bilayer nanoribbon flakes," *Journal of Physical Chemistry C*, vol. 119, no. 18, pp. 10 076–10 084, 2015.

[117] M. Fleischmann, R. Gupta, D. Weckbecker, W. Landgraf, O. Pankratov, V. Meded, and S. Shallcross, "Moiré edge states in twisted graphene nanoribbons," *Physical Review B*, vol. 97, no. 20, p. 205128, 2018.

[118] J. Liu, J. Liu, and X. Dai, "Pseudo landau level representation of twisted bilayer graphene: Band topology and implications on the correlated insulating phase," *Physical Review B*, vol. 99, no. 15, p. 155415, 2019.

[119] K. Wakabayashi, M. Fujita, H. Ajiki, and M. Sigrist, "Electronic and magnetic properties of nanographite ribbons," *Physical Review B*, vol. 59, pp. 8271–8282, Mar 1999.

[120] T. Kato, "On the adiabatic theorem of quantum mechanics," *Journal of the Physical Society of Japan*, vol. 5, no. 6, pp. 435–439, 1950.

[121] V. Fock, "Über die beziehung zwischen den integralen der quantenmechanischen bewegungsgleichungen und der schrödingerschen wellengleichung," *Zeitschrift für Physik*, vol. 49, no. 5, pp. 323–338, 1928.

[122] D. Xiao, M.-C. Chang, and Q. Niu, "Berry phase effects on electronic properties," *Review Modern Physics*, vol. 82, pp. 1959–2007, Jul 2010.

[123] B. Simon, "Holonomy, the quantum adiabatic theorem, and berry's phase," *Physical Review Letters*, vol. 51, pp. 2167–2170, Dec 1983.

[124] G. Ortiz and R. M. Martin, "Macroscopic polarization as a geometric quantum phase: Many-body formulation," *Physical Review B*, vol. 49, pp. 14 202–14 210, May 1994.

[125] R. D. King-Smith and D. Vanderbilt, "Theory of polarization of crystalline solids," *Physical Review B*, vol. 47, pp. 1651–1654, Jan 1993.

[126] R. Resta, "Theory of the electric polarization in crystals," *Ferroelectrics*, vol. 136, no. 1, pp. 51–55, 1992.

[127] P. Streda, "Theory of quantised hall conductivity in two dimensions," *Journal of Physics C: Solid State Physics*, vol. 15, no. 22, p. L717, aug 1982.

[128] D. R. Hofstadter, "Energy levels and wave functions of bloch electrons in rational and irrational magnetic fields," *Physical Review B*, vol. 14, pp. 2239–2249, Sep 1976.

[129] H. Schulz-Baldes, J. Kellendonk, and T. Richter, "Simultaneous quantization of edge and bulk hall conductivity," *Journal of Physics A: Mathematical and General*, vol. 33, no. 2, p. L27, jan 2000.

[130] S. Ryu and Y. Hatsugai, "Topological origin of zero-energy edge states in particle-hole symmetric systems," *Physical Review Letters*, vol. 89, p. 077002, Jul 2002.

[131] X.-L. Qi, Y.-S. Wu, and S.-C. Zhang, "General theorem relating the bulk topological number to edge states in two-dimensional insulators," *Physical Review B*, vol. 74, p. 045125, Jul 2006.

[132] T. Nakanishi and T. Ando, "Conductance of crossed carbon nanotubes," *Journal of the Physical Society of Japan*, vol. 70, no. 6, pp. 1647–1658, 2001.

[133] S. Uryu, "Electronic states and quantum transport in double-wall carbon nanotubes," *Physical Review B*, vol. 69, p. 075402, Feb 2004.

[134] J. C. Slater and G. F. Koster, "Simplified lcao method for the periodic potential problem," *Physical Review*, vol. 94, pp. 1498–1524, Jun 1954.

[135] A. M. Popov, I. V. Lebedeva, A. A. Knizhnik, Y. E. Lozovik, and B. V. Potapkin, "Commensurate-incommensurate phase transition in bilayer graphene," *Physical Review B*, vol. 84, no. 4, p. 045404, 2011.

[136] K. Uchida, S. Furuya, J.-I. Iwata, and A. Oshiyama, "Atomic corrugation and electron localization due to moiré patterns in twisted bilayer graphenes," *Physical Review B*, vol. 90, p. 155451, Oct 2014.

[137] M. Van Wijk, A. Schuring, M. Katsnelson, and A. Fasolino, "Relaxation of moiré patterns for slightly misaligned identical lattices: graphene on graphite," *2D Materials*, vol. 2, no. 3, p. 034010, 2015.

[138] S. Dai, Y. Xiang, and D. J. Srolovitz, "Twisted bilayer graphene: Moiré with a twist," *Nano letters*, vol. 16, no. 9, pp. 5923–5927, 2016.

[139] S. K. Jain, V. Juričić, and G. T. Barkema, "Structure of twisted and buckled bilayer graphene," *2D Materials*, vol. 4, no. 1, p. 015018, 2016.

[140] N. N. T. Nam and M. Koshino, "Lattice relaxation and energy band modulation in twisted bilayer graphene," *Physical Review B*, vol. 96, p. 075311, Aug 2017.

[141] I. V. Lebedeva, A. A. Knizhnik, A. M. Popov, Y. E. Lozovik, and B. V. Potapkin, "Interlayer interaction and relative vibrations of bilayer graphene," *Physical Chemistry Chemical Physics*, vol. 13, no. 13, pp. 5687–5695, 2011.

[142] T. Gould, S. Lebègue, and J. F. Dobson, "Dispersion corrections in graphenic systems: a simple and effective model of binding," *Journal of Physics: Condensed Matter*, vol. 25, no. 44, p. 445010, 2013.

[143] L. Brown, R. Hovden, P. Huang, M. Wojcik, D. A. Muller, and J. Park, "Twinning and twisting of tri-and bilayer graphene," *Nano letters*, vol. 12, no. 3, pp. 1609–1615, 2012.

[144] J. Lin, W. Fang, W. Zhou, A. R. Lupini, J. C. Idrobo, J. Kong, S. J. Pennycook, and S. T. Pantelides, "Ac/ab stacking boundaries in bilayer graphene," *Nano letters*, vol. 13, no. 7, pp. 3262–3268, 2013.

[145] J. S. Alden, A. W. Tsen, P. Y. Huang, R. Hovden, L. Brown, J. Park, D. A. Muller, and P. L. McEuen, "Strain solitons and topological defects in bilayer graphene," *Proceedings of the National Academy of Sciences*, vol. 110, no. 28, pp. 11 256–11 260, 2013.

[146] M. Koshino, "Interlayer interaction in general incommensurate atomic layers," *New Journal of Physics*, vol. 17, no. 1, p. 015014, jan 2015.

[147] M. Koshino and P. Moon, "Electronic properties of incommensurate atomic layers," *Journal of the Physical Society of Japan*, vol. 84, no. 12, p. 121001, 2015.

[148] D. Weckbecker, S. Shallcross, M. Fleischmann, N. Ray, S. Sharma, and O. Pankratov, "Low-energy theory for the graphene twist bilayer," *Physical Review B*, vol. 93, p. 035452, Jan 2016.

[149] Y. Cao, J. Y. Luo, V. Fatemi, S. Fang, J. D. Sanchez-Yamagishi, K. Watanabe, T. Taniguchi, E. Kaxiras, and P. Jarillo-Herrero, "Superlattice-induced insulating states and valley-protected orbits in twisted bilayer graphene," *Physical Review Letters*, vol. 117, p. 116804, Sep 2016.

[150] R. Ribeiro-Palau, C. Zhang, K. Watanabe, T. Taniguchi, J. Hone, and C. R. Dean, "Twistable electronics with dynamically rotatable heterostructures," *Science*, vol. 361, no. 6403, pp. 690–693, 2018.

[151] M. Dienwiebel, G. S. Verhoeven, N. Pradeep, J. W. M. Frenken, J. A. Heimberg, and H. W. Zandbergen, "Superlubricity of graphite," *Phys. Rev. Lett.*, vol. 92, p. 126101, Mar 2004.

[152] Z. Liu, J. Yang, F. Grey, J. Z. Liu, Y. Liu, Y. Wang, Y. Yang, Y. Cheng, and Q. Zheng, "Observation of microscale superlubricity in graphite," *Phys. Rev. Lett.*, vol. 108, p. 205503, May 2012.

[153] T. Cea, N. R. Walet, and F. Guinea, "Twists and the electronic structure of graphitic materials," *Nano letters*, vol. 19, no. 12, pp. 8683–8689, 2019.

[154] M. Fujimoto, H. Koschke, and M. Koshino, "Topological charge pumping by a sliding moiré pattern," *Physical Review B*, vol. 101, p. 041112, Jan 2020.

[155] Y. Zhang, Y. Gao, and D. Xiao, "Topological charge pumping in twisted bilayer graphene," *Physical Review B*, vol. 101, no. 4, p. 041410, 2020.

[156] Y. Su and S.-Z. Lin, "Topological sliding moiré heterostructure," *Physical Review B*, vol. 101, no. 4, p. 041113, 2020.

[157] M. Mucha-Kruczyński, J. R. Wallbank, and V. I. Fal'ko, "Heterostructures of bilayer graphene and h-bn: Interplay between misalignment, interlayer asymmetry, and trigonal warping," *Physical Review B*, vol. 88, p. 205418, Nov 2013.

[158] J. Jung, A. Raoux, Z. Qiao, and A. H. MacDonald, "Ab initio theory of moiré superlattice bands in layered two-dimensional materials," *Physical Review B*, vol. 89, p. 205414, May 2014.

[159] M. H. Naik and M. Jain, "Ultraflatbands and shear solitons in moiré patterns of twisted bilayer transition metal dichalcogenides," *Physical Review Letters*, vol. 121, p. 266401, Dec 2018.

[160] C. Jin, E. C. Regan, A. Yan, M. Iqbal Bakti Utama, D. Wang, S. Zhao, Y. Qin, S. Yang, Z. Zheng, S. Shi *et al.*, "Observation of moiré excitons in wse2/ws2 heterostructure superlattices," *Nature*, vol. 567, no. 7746, pp. 76–80, 2019.

[161] E. M. Alexeev, D. A. Ruiz-Tijerina, M. Danovich, M. J. Hamer, D. J. Terry, P. K. Nayak, S. Ahn, S. Pak, J. Lee, J. I. Sohn *et al.*, "Resonantly hybridized excitons in moiré superlattices in van der waals heterostructures," *Nature*, vol. 567, no. 7746, pp. 81–86, 2019.

[162] H. Yu, G.-B. Liu, J. Tang, X. Xu, and W. Yao, "Moiré excitons: From programmable quantum emitter arrays to spin-orbit–coupled artificial lattices," *Science advances*, vol. 3, no. 11, p. e1701696, 2017.

[163] R. Wang, P. Wang, K. Zhang, and Z. Song, "Moiré pattern of a spin liquid and a néel magnet in the kitaev model," *Physical Review B*, vol. 102, no. 9, p. 094207, 2020.

[164] T. Wang, N. F. Yuan, and L. Fu, "Moiré surface states and enhanced superconductivity in topological insulators," *Physical Review X*, vol. 11, no. 2, p. 021024, 2021.

[165] S. Kezilebieke, V. Vano, M. N. Huda, M. Aapro, S. C. Ganguli, P. Liljeroth, and J. L. Lado, "Moiré-enabled topological superconductivity," *Nano letters*, vol. 22, no. 1, pp. 328–333, 2022.

[166] Y.-H. Li and R. Cheng, "Moiré magnons in twisted bilayer magnets with collinear order," *Physical Review B*, vol. 102, no. 9, p. 094404, 2020.

[167] M. Akram, H. LaBollita, D. Dey, J. Kapeghian, O. Erten, and A. S. Botana, "Moiré skyrmions and chiral magnetic phases in twisted crx3 (x= i, br, and cl) bilayers," *Nano Letters*, vol. 21, no. 15, pp. 6633–6639, 2021.

List of publication

- Paper I

Diamagnetic levitation and thermal gradient driven motion of graphite

Manato Fujimoto, and Mikito Koshino

Physical Review B **100**, 045405 (2019)

- Paper II

Topological charge pumping by sliding moiré pattern

Manato Fujimoto, Henri Koschke, and Mikito Koshino

Physical Review B **101**, 041112(R) (2020)

- Paper III

Moiré edge states in twisted bilayer graphene and their topological relation to quantum pumping

Manato Fujimoto, and Mikito Koshino

Physical Review B **103**, 155410 (2021)

- Paper IV

Effective continuum model of twisted bilayer GeSe and origin of the emerging one-dimensional mode

Manato Fujimoto and Toshikaze Kariyado

Physical Review B **104**, 125427 (2021)

- Paper V

Perfect one-dimensional interface states in a twisted stack of three-dimensional topological insulators

Manato Fujimoto, Takuto Kawakami, and Mikito Koshino

Physical Review Research **4**, 043209 (2022)

- Paper VI

Mixed-dimensional moiré systems of graphitic thin films with a twisted interface

Dacen Waters, Ellis Thompson, Esmeralda Arreguin-Martinez, Manato Fujimoto, Yafei Ren, Kenji Watanabe, Takashi Taniguchi, Ting Cao, Di Xiao, Matthew Yankowitz

arXiv preprint arXiv:2211.15606 (2022)

This thesis is mainly based on Paper II and Paper III.

Acknowledgments

I am deeply grateful to my supervisor, Prof. Mikito Koshino, for his invaluable advice, unwavering support, and boundless patience throughout my Ph.D. studies. His expertise and guidance have been instrumental in my understanding and success in research. I am unable to find adequate words to express my appreciation for him. I would also like to extend my gratitude to Prof. Kenichi Asano, Prof. Jobu Matsuno, Prof. Kazutaka Kudo, and Prof. Takuto Kawakami for serving on my committee and providing insightful comments on my thesis. In particular, I am especially appreciative of Prof. Takuto Kawakami for our productive discussions and valuable feedback.

I am also thankful to Prof. Kazuhiko Kuroki and Prof. Masayuki Ochi for accepting me as a short-time student during my undergraduate studies. I am indebted to Dr. Kariyado for welcoming me as an intern at the National Institute for Materials Science and for the opportunity to engage in collaborative research. I am grateful to Prof. Di Xiao and his group for welcoming me as a visiting student and for the chance to collaborate with him and Prof. Matthew Yankowitz.

I am grateful to Mr. Naoto Nakatsuji for introducing me to the field of twisted bilayer graphene and for several discussions. I also extend my thanks to Mr. Hitomi Masaru for creating a lively atmosphere in the Koshino group. My appreciation also goes to the secretaries, Ms. Mari Homma and Ms. Yuki Harada, for their support outside of research and other endeavors. I am also thankful to the Interactive Cadet Program for providing the opportunity to visit the National Institute for Materials Science and the University of Washington. I am also thankful to Prof. Kenji Iijima and the secretaries, Ms. Miwa Shimizu, Ms. Aki Okubo, and Ms. Yasuko Ueda, for providing me with ample time for meaningful conversations.

Lastly, I would like to express my deepest gratitude to my parents, Mayumi Fujimoto and Junzo Fujimoto, for their unwavering support throughout my life and for providing me with a chance to challenge my Ph.D.